Politecnico di Torino

Master's Degree in Energy and Nuclear Engineering

Politecnico
di Torino

Master's Degree Thesis

Annual simulation of hybrid CSP-PV solar plants: thermal performance and techno-economic analysis

Supervisor:
Roberto Bonifetto

Candidate:
Matteo Basso

Co-Supervisor:
Roberto Zanino

External Supervisor:
Mattia Cagnoli

March 17^{th}, 2025

Abstract

In a scenario where renewable technologies are gaining more and more momentum, this work investigates computationally optimized solutions to an existing CSP plant virtual model, created using the Modelica language, with the final purpose of extending the simulation scope from short transients to an entire typical year. After identifying the most relevant sources of complexity, namely the heat storage units and the receiver tube, the focus has been directed towards the simplification of the way such elements were modeled, trying to ensure the best balance between accuracy and computational cost. For what concerns the storage tanks, it was discovered that heat losses had a marginal influence on major parameters like heat transfer fluid temperature, though constituted a significant burden from the numerical point of view, so they were decided to be neglected. The receiver tube, instead, originally implemented a bi-dimensional discretization in order to guarantee more accurate results, which was removed for time optimization purposes. The final versions were initially tested over a single day, where they proved able to guarantee run time reductions between 90% and 95%, still maintaining excellent levels of accuracy. This outcome enabled the execution of simulations over an entire typical year in reasonable amounts of time, around 4 to 5 minutes. Unlike the data obtained from the original short-term simulations, such a result provides meaningful values constituting a reliable starting point for what concerns financial evaluations, LCOE projections under different scenarios, and plant performance predictions. Additionally, the final model was successfully employed in an hybridized configuration in order to assess its capabilities of supporting possible integrations with alternative renewable power systems.

Contents

List of Figures

List of Tables

Chapter 1

Introduction

The ongoing process of decarbonization of the energy sector has been generating an escalation in the integration of intermittent renewable sources like photovoltaic and wind, which have experienced a remarkable growth in recent years. Their inherent intermittency, on the other hand, coupled with the rising reliance the energy market has on them, poses a significant challenge to grid stability and reliability, requiring the consideration of dispatchability metrics beyond the mere cost of electricity. In this context, Concentrated Solar Power (CSP) emerges as a promising solution, offering a sustainable and environmentally sound pathway to meeting both electrical and thermal energy demands. Unlike PV and wind, in addition, the CSP technology, when integrated with advanced thermal energy storage systems, results able to provide a controlled power output throughout the whole day, aligning supply with demand fluctuations and ensuring stable generation even during periods of low solar irradiance or nighttime. This intrinsic dispatchability, coupled with the potential for hybridization with fossil fuels or other renewable energy systems, makes CSP a critical technology for achieving a carbon-neutral electric grid, addressing the limitations of intermittent renewables and contributing to the broader objective of a sustainable energy future.

1.1 Solar power

The Sun is the star at the center of the Solar System, a sphere characterized by a 1 392 000 km long diameter and a mass of $1.99 \cdot 10^{30}$ kg and featuring a layered structure consisting of core, radiative zone, convective zone, photosphere, chromosphere, and corona. The center of the Sun is constituted by the core, where the incredibly high pressures and temperatures (around 15 000 000 K) trigger nuclear fusion processes in which hydrogen, which makes up about 75% of the solar mass, is converted into helium, rep-

resenting instead 23% of it [1]. The most important reaction involved is the so-called proton-proton reaction chain that, overall, can be described by the following equation:

$$4p^+ \rightarrow {}^4He^{2+} + 2e^+ + 2v + \Delta mc^2 \tag{1.1}$$

Equation 1.1 describes the fusion of protons (hydrogen nuclei, p^+) into helium (${}^4He^{2+}$), which involves the additional release of positrons (e^+) and neutrinos (v), as well as the conversion of a mass fraction into 26.7 MeV of energy per reaction (around $4.3 \cdot 10^{-12}$ J). Considering that the total solar mass defect pace amounts to $4.3 \cdot 10^9$ kg/s, the corresponding emitted radiative power (P_S) results $3.85 \cdot 10^{26}$ W, part of which gets released as radiation of matter, namely solar winds, but most of it as electromagnetic radiation resembling the spectrum and the intensity of the radiation of a black body at 5777 K [12].

A fraction of this power, named "solar constant", traveling through space at the speed of light, reaches the Earth's atmospheric surface and constitutes the energy source for CSP plants operation. By using the energy conservation principle, it can be stated that the radiative power emitted from the Sun gets evenly distributed on the virtual sphere, centered on the Sun, around which the Earth orbits. This means that, given the average distance between the Earth and the Sun r_{SE}, assumed equal to $1.496 \cdot 10^{11}$ m, the solar constant G_{SC}, corresponding to "the radiant power per square meter incident on a surface on top of the atmosphere and in normal direction to the incident rays" [12], can be calculated as:

$$G_{SC} = \frac{P_S}{4\pi \cdot {r_{SE}}^2} = \frac{3.85 \cdot 10^{26}}{4\pi \cdot (1.496 \cdot 10^{11})^2} = 1367 \frac{W}{m^2} \tag{1.2}$$

At this point, in order to get the total amount of power $\dot{Q}_E$ the Earth receives from the Sun, the solar constant G_{sc} must be multiplied by the terrestrial cross section area, taking its mean radius r_E equal to 6371 km [12]. The result is the following:

$$\dot{Q}_E = \pi \cdot r^2 \cdot G_{sc} = \pi \cdot (6371 \cdot 10^3)^2 \cdot 1367 = 1.74 \cdot 10^{17} W \tag{1.3}$$

[1] The remaining 2% is constituted by heavier elements that include oxygen, carbon, neon, and iron.

Integrating this value over an entire year, the total solar energy Q_E received by the Earth is:

$$Q_E = \int \dot{Q}_E \cdot dt = 1.74 \cdot 10^{17} \cdot 8760 = 1.52 \cdot 10^{18} kWh \tag{1.4}$$

This value might convey no particular information by itself, but when compared to the world primary energy supply, which added up to a total of $1.76 \cdot 10^{14}$ kWh in 2022 [19], this result becomes impressive. What these numbers say is that the Sun provides the Earth with more than 8636 times the energy the whole humanity needs actually for its primary energy consumption [12]. These values provide a global average annual energy yield of:

$$Q_{E,spec} = \frac{Q_E}{4\pi \cdot r^2} = \frac{1.52 \cdot 10^{18}}{4\pi \cdot (6371 \cdot 10^3)^2} = 2980 \frac{kWh}{m^2} \tag{1.5}$$

It has to be considered, though, that the value of irradiance considered is referred to measurements performed outside the atmosphere. Many different attenuating factors intervene, indeed, between the atmosphere and the surface, which are generally grouped into two classes: absorption and scattering. The first consists of a process performed by some atmospheric constituents, among which ozone, water vapor, carbon dioxide, oxygen, and nitrogen, which absorb radiation of some specific spectral ranges, reducing the energy photons are able to provide. The second, instead, is a process in which radiation is deviated from a straight propagation by atoms and molecules (Rayleigh scattering), or water droplets, ice crystals, and aerosol particles (Mie scattering). This mechanism does not generate any energy dissipation, but reduces the share of beam radiation reaching the terrestrial surface, which is the only one CSP systems can exploit. It has to be noted how the intensity of such radiation extinction processes is highly variable and depends on several factors like location, weather conditions, urbanization level, and many more, so the definition of a single global indicator defining DNI (Direct Normal Irradiation) at ground level is impossible [12]. Figure 1.1 provides information on yearly energy yield per unit square meter across the whole globe, which can be compared with Equation 1.5 to assess discrepancies between theoretical and real values.

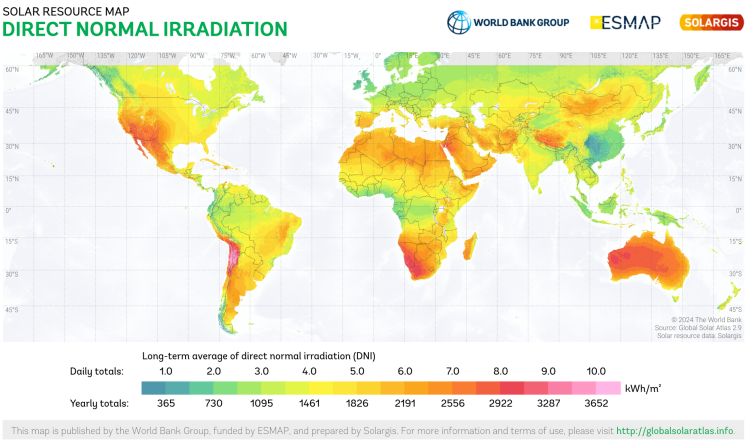

Figure 1.1: Solar resource map [10]

1.2 CSP technology

Concentrating Solar Power, also known as CSP, stands out as a promising technology for countries characterized by high irradiance and clear skies, like sub- and over-equatorial bands (see Figure 1.1). Its electrical output, similarly to photovoltaic technologies, well matches the electrical daily demand in places where air-conditioning systems are spreading. What's more, CSP plants can be coupled with heat storage units or fossil-fueled backup systems, guaranteeing dispatchability even when clouds block the sun or after sundown. These elements make the concentrated solar power solution an environmentally-friendly alternative to coal-based power plants for base loads, as well as a valid competitor to PV and wind technologies, able to guarantee greater flexibility and a steadier energy generation, less related to source fluctuations. The exploitation of high temperature heat transfer fluids, in addition, makes CSP potentially able to drive secondary processes like high-temperature heat production for industrial processes, co-generation of heating, cooling, and power, as well as water desalination [1].

The operation of a general CSP plant is based on a sequence of energy transformations that ultimately produce electrical energy. The energy conversion process begins with the concentration of direct solar radiation by means of components called reflectors, which is subsequently used to increase the heat transfer fluid temperature within the receiver. The medium can either be directly used to generate high-pressure steam by means of an heat exchanger, or alternatively stored in a heat storage system for later use. The pressurized gas drives a steam turbine, where the thermal energy is converted into kinetic energy. Finally, the rotational motion of the turbine is converted into electrical energy through an electric generator, which supplies power to the electrical grid.

The four most important CSP technologies are described in the following Subsections.

1.2.1 Parabolic trough

Parabolic trough power plants represent the most widespread solution currently in adoption for CSP plants, constituting more than 90% of the systems in operation and under construction, as well as more than 50% of the projects planned. These systems make use of parabolic trough collectors in order to focus solar radiation on the surface of a cylindrical receiver inside which the heat transfer fluid flows [13].

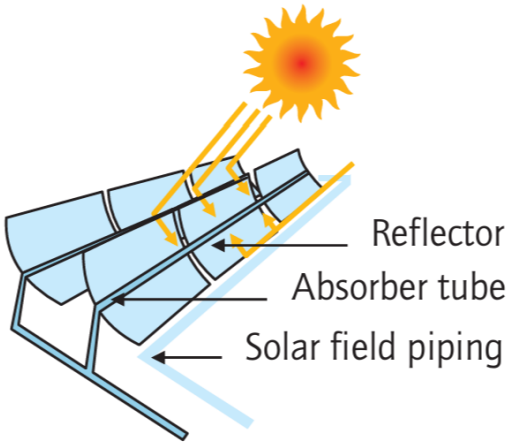

Figure 1.2: Parabolic trough [1]

The following lines present the most characterizing key components this technology makes use of.

Heat transfer fluid

In the parabolic trough power plants, heat transfer fluids should fulfill a set of minimum requirements, among which:

- liquid under operational conditions;
- sufficiently high evaporation temperature;
- low freezing point;
- high thermal stability;
- high high specific heat capacity and thermal conductivity;
- low viscosity;

- low costs;

- environmentally friendly and safe.

The three most commercially relevant heat transfer mediums are presented below.

- *Synthetic thermo oil:* also called "thermo oil", the synthetic thermo oil is a mixture of biphenyl and diphenyl oxides with a long history of usage in the CSP industry. It is characterized by an abundant availability, as well as particularly favorable physical and thermal characteristics: its freezing point is 12 °C, well below room temperature, and presents a quite high specific heat capacity. On the other side, though, this medium has some drawbacks among which a limited maximum operative temperature, around 400 °C, a periodical need for replacement due to aging processes, relatively high costs, environmentally dangerous. In addition, it results unsuitable for the exploitation as heat storage medium [13].

- *Mineral oil:* it was once used as heat transfer fluid due to its employability as bot heat transfer fluid and thermal storage medium, but has been eventually substituted by thermo oil due to its limited operational maximum temperature, which is slightly above 300 °C [13].

- *Molten salt:* even if their usage is today still under investigation, molten salts mixtures present several advantages over synthetic oil, the most important of which are represented by the higher temperatures it can reach before degrading, which range between 450 and 550 °C, and the possibility to be directly implemented as storage medium. The higher temperatures allow higher Rankin cycle efficiencies along with smaller storage sizes for a given capacity. Cheaper than thermo oil, they also result environmentally friendlier, non-toxic, and non-flammable. A downside is instead represented by the high freezing point, which stands between 120 and 220 °C [13].

Collector

Parabolic trough power plants utilize parabolic collectors whose shape is a symmetrical section of a parabola around its vertex. These elements are thereby characterized by a focal line, which is defined by the collection of focal points along their parabolic cross-sections. The incoming radiation, whose direction can be approximated to parallel to the optical plane, is reflected in such a manner that it converges along this focal line, consequently enabling an efficient concentration of solar energy. Mirrors usually employ silver coated glass, a multi-layered material which grants optimal levels of

reflectivity in the solar spectrum band, and are characterized by high stiffness and impeccable surface accuracy, which result necessary elements for precise Sun tracking and high concentration ratios [13].

Receiver

The receivers in parabolic trough power plants serve the critical function of converting concentrated solar radiation into heat and transferring this thermal energy to the piping system, which subsequently delivers it to the power block. Efficient energy conversion requires high radiation absorption and minimal heat losses. In the case of the absorber tube, this is obtained through the exploitation of a combination of selective coatings called CERMET. These layers allow to obtain high absorptance in the solar spectral range (250 nm $\leq \lambda \leq$ 2500 nm, where λ indicates the radiation wavelength), and low emissivity in the infrared range (3000 nm $\leq \lambda \leq$ 50 000 nm). This feature allows the receiver to effectively absorb solar radiation, simultaneously minimizing the HTF re-emitted heat fraction exchanged with the external environment. Additionally, the absorber tube is shielded by a glass sheath, which prevents air from flowing around it, resulting in reduced heat losses. In order to further minimize convection, the glass body could also be evacuated [13].

Sun tracking system

Parabolic troughs must track the Sun to ensure continuous concentration of direct solar radiation. Similarly to other line-concentrating collectors, they employ a single-axis tracking system, in contrast to point-concentrating systems, which require instead two-axis tracking. The tracking motion is permitted by drive units, each one dedicated to a single collector assembly, consisting of a series of interconnected collector modules. Given that these assemblies can be extensive in length, every unit must possess sufficient strength to seamlessly maneuver such large structures and to maintain their alignment, even under potentially demanding wind conditions [13].

Parabolic trough plants usually exploit synthetic thermo oil as HTF and feature a rectangular, almost square, solar field, with capacities ranging from 30 to 80 MW. The power block is frequently situated at or close to the solar field's center, an arrangement that, together with the square shape, makes it feasible to minimize thermal losses by making the pipes as short as possible, minimizing the hot heat transfer medium path to the power block [13].

1.2.2 Linear Fresnel reflector

Linear Fresnel power plants represent the second type of line-focusing collector systems. While parabolic troughs represent the optically best solution

for concentrating radiation, providing, thanks to the parabolic geometry, the highest achievable concentration ratio and energy yield per aperture area, Fresnel reflectors represent a cheaper alternative, able to guarantee a lower LCOE, especially for low-sized power plants, and the highest land usage efficiency among different solar field solutions [11].

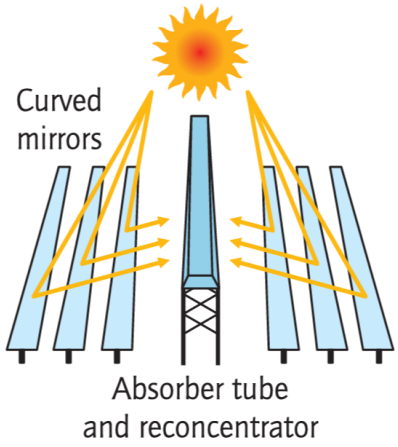

Figure 1.3: Linear Fresnel reflector [1]

Heat transfer fluid

The linear Fresnel mirrors technology makes use of the same HTF exploited by parabolic troughs.

Collector

Fresnel mirrors can be created by substituting a parabolic trough with multiple stripes of linear segments made of smaller and slightly curved reflectors that focus incident radiation onto the same focal line of the parabolic element. Obviously, for what concerns the capability to concentrate the incoming radiation along a focal line, Fresnel collectors have a similar effect compared to the corresponding parabolic trough, even though, due to the approximation introduced, the optical trajectories of corresponding rays after reflection are not exactly identical and the incidence angles in the focal plane slightly differ [11].

Receiver

Linear Fresnel systems present very different receiver structures compared to the parabolic trough technology. The absorber tube (or tubes), indeed,

are only composed of a CERMET coating coupled with metallic and anti-reflective layers, while the additional glass sheath, along with vacuum insulation, is absent. These elements are placed on rollers in order to compensate for significant thermal expansion phenomena, which cause steel receivers to reach longitudinal elongations up to 0.6% at high operational temperatures. An additional element characterizing Fresnel receivers is the so-called "secondary concentrator" that, in order to mitigate the unavoidable optical inaccuracy of the Fresnel tube and to improve the intercept factor, provides a reflecting surface above the collector in order to re-direct a share of the radiation that is not precisely oriented to the focal line. The upper side of this coverage, in addition, provides a thermal insulation layer to minimize losses behind the mirror, as well as protecting the collector against the weather. Its lower side is instead sealed with a low infrared and high solar spectral range transmittance glass panel in order to increase heat absorption and retention. It can have a compound parabolic shape in the case of single absorbers, or a trapezoidal shape for multi-tube configurations [11].

Tracking system

Fresnel collectors present a single-axis tracking system, but compared to parabolic troughs, it has the advantage of requiring sensibly lower forces to move the mirrors. These elements, in fact, are much smaller and lighter compared to their parabolic counterparts, and the mirror structure can be easily designed so that the center of gravity is within the rotational axis, allowing for a reduction in motor requirements and gears complexity [11].

Until now, due to the unavailability of large size operative plants, no significant data is available for Fresnel power systems. In order to compare them with the parabolic troughs alternative, then, in 2004 the ISE Fraunhofer Institute of Freiburg made a simulation comparing two 50 MW power plants exploiting such technologies. While solar field costs were determined as being 220 EUR/m^2 for the parabolic trough power plant and 150 for the Fresnel power plant, the electricity generated by the parabolic trough resulted characterized by an LCOE between +8% and +17% higher than the one obtained in a Fresnel power plant. More specifically, greater differences were obtained where radiation conditions were weak, since a more extended solar field resulted necessary to reach the target power, while higher DNIs reduced the spread in LCOE values. In the year 2009, DLR assessed that linear Fresnel plant should feature specific investment costs around 55% of the ones characterizing parabolic trough fields in order to reach the same LCOE and result cost-competitive with the rival technology [11].

1.2.3 Solar tower

A solar tower power plant, also called "central receiver", consists of a field composed of a multitude of Sun-tracking mirrors that reflect solar radiation onto a receiver located at the top of a structure called "solar tower", where the energy is transferred to the heat transfer fluid. This type of solution, called "point focus" or "point concentration", is able to reach concentration ratios that are well above the values characterizing line-focusing techniques, and therefore has the potential to get the medium to very high operational temperatures, which unlock possible side applications such as hydrogen production or seawater desalination [16].

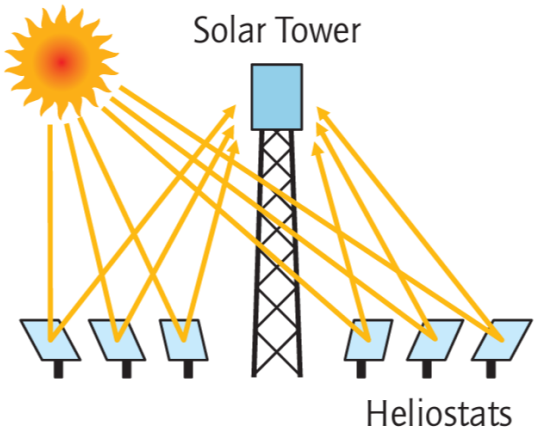

Figure 1.4: Solar tower [1]

Heat transfer fluid

Central receiver power plants, due to their higher operational temperature, make use of molten salts mixtures or air.

Solar field

A typical solar field is made up of so-called "heliostats", mirrors provided with a two-axis tracking system designed to track the solar path in time, continuously directing radiation towards the central receiver. The important size of such mirrors, ranging up to 150 m^2, coupled with the necessity to guarantee a satisfying optical performance even under demanding wind loads, requires the implementation of stiff metallic structures and powerful driving systems that, coupled with the high number of units typically employed (from hundreds to several thousands), make the heliostat field one of the major voices in a solar plant investment, constituting around 50% of

it. Mirrors are spread in front of or even all around the tower up to a distance of approximately 1000 m in order to maximize irradiance collection, still keeping atmospheric attenuation and spillage losses under control. The specific design of the field is determined with the target of minimizing land usage and investment costs given the required power generation. Another important aspect related to this component is the aiming strategy, whose ultimate purpose is to guarantee that irradiance gets distributed as evenly as possible on the receiver's surface. The most widespread aiming strategies include single aim point, one- or two-dimensional smart aiming, and single or double aim point at the lower part of the receiver [16].

Receiver

Embodying the most crucial component of the whole power system, the receiver has the function to absorb the concentrated solar energy coming from the heliostat field and transfer it to the working fluid. There are four main technologies characterizing it [16]:

- *Direct absorption (falling particle) receiver:* this component makes use of a cavity inside of which is generated a curtain of falling solid salt particles, which get heated up by the radiation directed through a sort of window. The medium, which reaches temperatures up to 2000 °C, gets stored and then used in an heat exchanger to transfer their energy to a selected heat transfer fluid.

- *External tube receiver:* this configuration involves a receiver externally provided with many vertically arranged pipes through which the heat transfer fluid is pumped.

- *Cavity receiver:* similar to the previous configuration, this alternative involves adjacent vertical pipes which are instead placed inside a cavity to minimize convective and radiative losses. This type of receiver works with both liquid and gaseous HTFs.

- *Volumetric receiver:* this technology does not involve pipes, but the heat transfer fluid, which in this case is constituted by air, is absorbed by a porous structure. More specifically, light gets initially concentrated towards the receiver's surface, which heats up. Then, the heat is transferred to the ambient air trapped inside, which gets sucked by the porous receiver through some blowers and transferred to a steam generator or, alternatively, a storage system. Finally, the residual warm air is partly recirculated, and partly used to cool down the external structure. The distribution of heating inside the absorber module favors the development of lower temperatures, which in turn generate a reduced amount of losses.

The typical size of such plants is usually one order of magnitude greater than line-focusing collector systems and easily amounts to several hundreds of megawatts. Commercial plants like Crescent Dunes, Nevada, feature 110 MW of electrical power and a 10 hours thermal storage, covering a surface of 1.2 km^2 with 10 000 heliostats, but bigger constructions like Ivanpah, in California, or Ouarzazate, in Morocco, respectively reach values of 370 and 510 MW [6]. This type of power plants are able to heat up the heat transfer fluid to operative temperatures ranging between 550 and 1000 °C, which ensure high cycle efficiency, reason for which central tower plants are considered the most promising CSP technology in the coming years [16].

1.2.4 Parabolic dish

Also know as "solar dish" or "Stirling system", it consists of a stand-alone paraboloid-shaped reflector concentrating solar radiation onto its focal point, where a receiver is places. The concentration ratios that this system is able to reach are the highest among the other CSP technologies, reason why the receiver employs hydrogen or helium gases as heat transfer fluid, which get heated up to temperatures between 650 and 750 °C. Such high temperatures grant exceptional thermal performances and high levels of efficiency, theoretically around 32% [21].

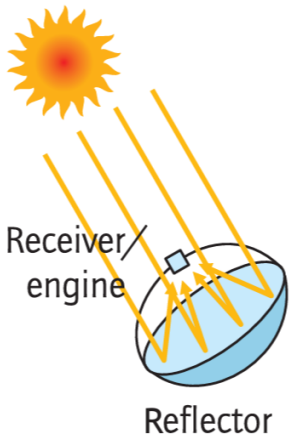

Figure 1.5: Parabolic dish [1]

On the other hand, though, the higher precision required for the parabolic dish and the Stirling engine, along with a sophisticated two-axis tracking system and limited industrial experience, make manufacturing and operational costs higher than other CSP technologies. In addition, the lack of thermal storage integration strongly limits parabolic dishes' ability to provide dispatchable power during periods of low solar irradiance [21].

1.3 Hybridization

"Hybridization" is a general term indicating the combination of different power generation technologies into a single system, and is usually implemented in order to maximize performance or compensate for potential flaws characterizing the individual unit. Typically, CSP plants get hybridized with [13]:

- *Fuel-fired backup heaters*, in order to increase capacity factor, reduce power gradients (or make them more controllable), maintain power generation under intermittent cloudiness conditions, equilibrate day-and-night rhythms, and cover peaks of demand.
- *Fuel-fired burner*, operated continuously during sunshine operations to increase heat transfer fluid temperature levels and enhance power block efficiency.
- *Fuel-based power plants*, where the solar system acts as a secondary power source and provides additional heat to the steam cycle.

In spite of providing substantial benefits to the power system as a whole, the just-mentioned hybridized alternatives all involve the exploitation of fossil-fuel-based units, a solution which goes in the completely opposite direction to climate neutrality. A promising alternative that has recently been studied involves the integration of PV and CSP technologies into a fully renewable hybrid solar-based power plant. Photovoltaic, wind turbines, and concentrated solar power technologies are not able to provide a continuous electrical supply and need to be coupled with energy storage systems to extend their dispatchability. While the Thermal Energy Storage (TES) units implemented in CSP plants result relatively cheap, the batteries needed for PV systems are currently very expensive, which makes dispatchable photovoltaic plants economically unviable. On the other hand, though, the complexity and costs related to CSP components and operations make this technology financially uncompetitive without incentives. Combining the strengths of these two systems, however, might represent a valid solution to the creation of an economically competitive and environmentally sustainable power plant, able to generate electricity with high levels of dispatchability [15].

The hybridization of PV and CSP can be achieved according to different levels of integration of the two technologies [15]:

- *Grid-level integration:* this type of solution involves the parallel operation of two separate plants, which are virtually aggregated as a single unit at the grid connection point, but are not able to transfer energy between each other.

- *Technology-level integration:* in this case the two plants result able to physically transfer energy between their components, with the PV side either supplying electricity to CSP auxiliaries or, for deeper integration levels, running CSP electric heaters or heat pumps in order to generate heat for the TES system.

- *Compact/Advanced integration:* this last solution makes use of PV-topping and spectral beam concepts to run both CSP and PV sections, maximizing their efficiency in the exploitation of solar radiation.

For what concerns CSP-PV integration, Subsection 3.4.3 will explore an hybridized version of the Partanna CSP site where, exploiting a technology-level integration, the electricity of the PV system will be used to heat up part of the HTF stored inside the TES units. The results obtained from such a configuration will be then compared to the CSP-only alternative in order to highlight potential advantages and disadvantages.

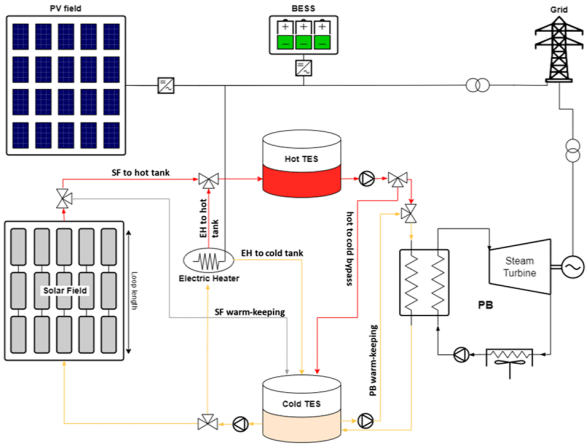

Figure 1.6: Hybrid CSP-PV layout [15]

A schematic general representation of such a solution, including a mirror field, a photovoltaic field, two TES units, respectively dedicated to the storage of high- and low-temperature HTF, an electric heater, a BESS system, an heat exchanger, and a power block running on a Rankine cycle, is provided by Figure 1.6.

Chapter 2

Scope

The starting point of this work is represented by a Concentrated Solar Power (CSP) plant model, specifically crafted to perform detailed simulations of the performance of its components in time, given the coordinates where the site is located and the evolution of climatic conditions in time.

The model has been developed in Modelica, "a language for modeling of cyber-physical systems, supporting acausal connection of components governed by mathematical equations to facilitate modeling from first principles" [2]. It makes available "object-oriented constructs that facilitate reuse of models, and can be used conveniently for modeling complex systems containing mechanical, electrical, electronic, magnetic, hydraulic, thermal, control, electric power or process-oriented subcomponents" [2]. This hierarchical organization makes the modeling of high-complexity systems much easier and intuitive, allowing single elemental components to be defined and tested independently before being incorporated into more elaborated structures. The open-source modeling and simulation environment that has been used is named "Open Modelica" [3].

The initial CSP model, designed to achieve the highest level of accuracy in results, requires thousands of equations to be described, so that it proves exclusively suitable for the simulation of short transients. Increasing too much the simulation window causes computation times to easily exceed a few hours, or even renders the model impossible to run, which represents a huge limitation to this tool. Extending its computation capabilities to larger time frames could make this model useful for additional evaluations like financial analysis, LCOE projections, scenarios evaluation, and many more, all requiring a pool of input data resulting more representative than a highly variable daily dataset.

The first step consisted of the analysis of the Modelica script in order to identify the CSP system structure and spot potential areas of improvement. Afterwards, different alternative stand-alone models were created and simulated over 24-hours time ranges in order to verify their correctness and

compare run times and trends related to the most significant indicators. Data analysis operations were performed in a Matlab environment. The models able to ensure the best balance between results accuracy and computational cost were then combined in order to maximize their performance, and consequently employed in the annual simulation of the whole concentrated solar power system. The following step consisted in the definition and test of an hybrid CSP-PV configuration able to provide an effective communication between the components characterizing the plant in response to external and internal signals.

Finally, the outcomes obtained from the different annual simulations were evaluated, compared, and then used to perform a techno-economic analysis with the ultimate purpose of computing the LCOE characterizing each alternative layout.

Chapter 3

Procedure

The reference plant considered in this study is the Partanna solar station, commissioned by FATA S.p.A. in the Italian province of Trapani, located on the west side of Sicily at a latitude of 37.70167° and longitude of 12.86389°.

This plant, in particular, implements the Linear Fresnel Reflector (LFR) technology and exploits a mixture of molten salts (60% $NaNO_3$, 40% KNO_3) as heat transfer fluid, whose properties can be found in Appendix B. The plant, in addition to the LFR system that makes up the so-called Solar Block (SB), is composed of a two-tank heat storage system consisting of a cold tank (CT) and a hot tank (HT), a gas-fired heater (GFH), two pump stations, and a salt-water heat exchanger that transfers the energy from the solar loop to a steam cycle in order to turn thermal energy into electricity. This last component will be referred to as Power Block (PB) [5].

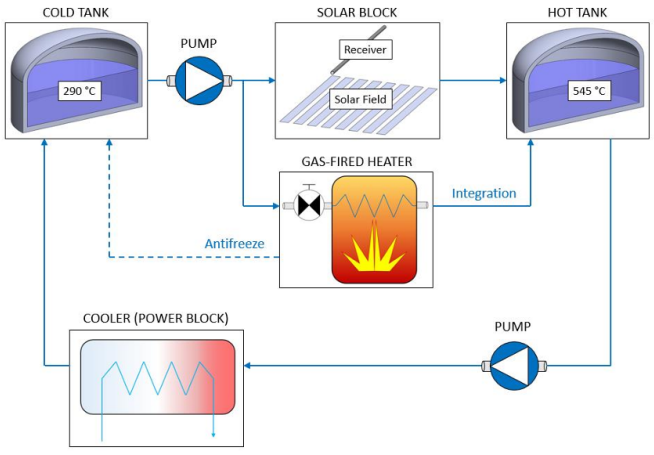

Figure 3.1: Solar station scheme [5]

Depending on local climatic conditions, the activity of pumps and GFH is regulated in order to keep the two tanks as close as possible to their design

temperature conditions: 563 K for the CT, corresponding to the receiver target inlet temperature, and 818 K for the HT, corresponding in this case to the receiver target outlet temperature.

The schematic representation is presented in Figure 3.1 highlights two different branches with the labels *Integration* and *Antifreeze*, which are referred to the two different possible configurations that the system can assume depending on environmental conditions. Let's analyze them more specifically:

- *Integration mode:* the GFH works in parallel with the SB, heating a share of 4.4 kg/s of molten salts coming out of the CT in order to provide the HT with an additional power that integrates the fraction coming from the LFR system.

- *Antifreeze mode:* designed for overnight operations, in this configuration the GFH heats a greater amount of the thermal vector (12.3 kg/s) pumped out of the CT up to about 653 K, sending it straight back to the CT to keep its temperature over a threshold of 533 K and prevent salts freezing. Since the temperature increase (563-653 K) is lower than the one required in the *Integration* mode (563-818 K), the mass flow rate deviated to the GFH, whose power of 1.8 MW is constant over time, results to be higher.

A more detailed conceptual scheme of the model, including a description of the main inputs, is shown in Figure 3.2.

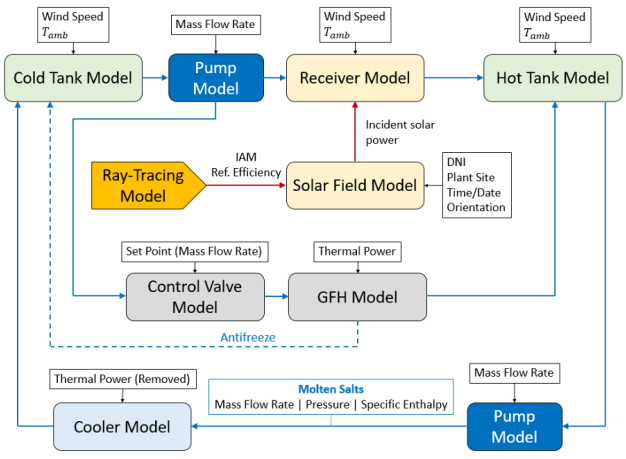

Figure 3.2: Solar station lumped-parameter scheme [5]

3.1 Original model

In this paragraph, the lumped-parameter thermal-fluid-dynamic models of the most important components making up the solar loop are briefly presented, considering as a reference the Partanna solar plant, whose details are reported in Appendix A. For more detailed information about the modeling of such blocks, refer to the technical report [5], which also provides the set of equations used to model the behavior of such sub-systems.

3.1.1 Thermal storage

The storage tank model has the purpose of calculating at every time step the level of molten salts inside the tank and the heat loss towards the external ambient, so as to define the insulation efficiency. The model includes the storage medium (molten salts), the inner metal walls, the outer insulation layer, the concrete basement, and the air layer between the top of the molten salts' free surface and the top of the tank, as shown in Figure 3.3. An aperture on the tank's roof ensures that the air layer is always at atmospheric pressure regardless of the amount of molten salts stored. The tank model is zero-dimensional, which means that it only considers a single average temperature for every component it is made of: no discretization in space is performed. The metal wall and the insulation layer are present in the tank's floor, roof, and lateral side, which have different thermal gradients due to an unequal interaction with the hot air and the molten salts, while the concrete basement characterizes only the bottom of the element. The main hypothesis assumed for the model are summarized below:

- The tank has a cylindrical shape and the curvature of the roof is not considered;
- The temperature of the ground under the basement is equal to the ambient temperature;
- The solar load on the outer tank surface is neglected since it is not concentrated;
- The air is considered to be transparent to the thermal radiation.

Figure 3.3 summarizes every heat transfer flux the model considers and, in particular, highlights the heat loss mechanisms:

- Convection and radiation towards the external ambient, which occur from the outer tank surfaces exposed to it;
- Conduction through the concrete basement towards the ground;

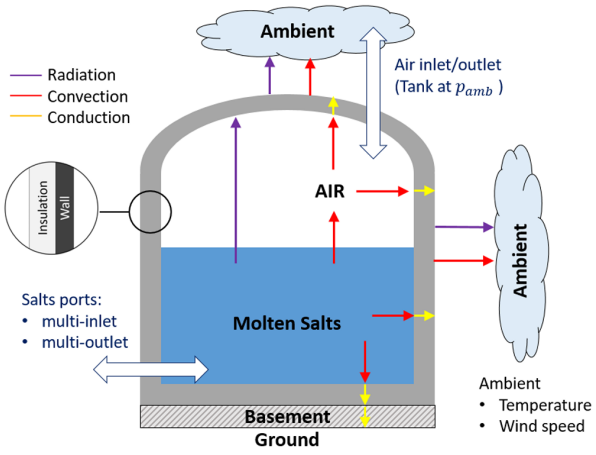

Figure 3.3: Thermal storage scheme [5]

- Release of hot air into the ambient, which occurs if the salts level increases, or inflow of fresh air (at ambient temperature) into the tank if the medium level decreases.

The required boundary conditions are wind speed and ambient temperature, while the initial conditions that need to be provided include molten salts level and temperature.

In order to better understand the simplifying procedures implemented in Section 3.2, the following Subsections will briefly provide a description of the Open Modelica models making up the thermal storage system.

PartialStorage

This model is dedicated to the resolution of the mass and momentum balance, while the energy balance is only partially completed. What is calculated, indeed, is an initial value of the medium's specific enthalpy, found after considering the current medium enthalpy and the different power flows at the inlets and outlets, which will subsequently be adjusted by taking into account the interactions with the air and the tank surfaces. What is also computed is the medium level inside the tank and the pressure at the level of every fluid port.

StorageHeat

This model extends the *PartialStorage* model by adding the calculation of the heat transfer with the boundaries, and in particular the convection between medium and bottom wall, and medium and side wall, and the radiation between medium and top wall. The temperature levels of such elements

are also defined here. The convective heat transfer between gas and medium and gas and walls is taken into account in a separate model.

GasModel

The considered model addresses the gas phase above the storage medium in the tank, computing the convective heat transfer between gas and tank (both the sides and the top), as well as gas and salts.

GasAmbModel

This model connects the *GasModel* with a *Boundary_pT* model that reproduces the external ambient conditions, allowing to properly take into account the properties of the air sucked into the tank when the level of the salts decreases.

Storage0D

The *Storage0D* block is the final Open Modelica description of a general tank, modeling the behavior of both the thermal medium stored inside and the different surfaces separating it from the external environment. It embeds the four sub-models seen previously and combines their results in order to provide comprehensive information about the molten salts and the thermal fluxes interacting with them.

The model (Figure 3.4) receives two input signals from the outer environment (blue arrows), namely ambient temperature and wind speed levels, which interact with the *GasModel* block (light blue circle), the *Boundary_pT* block (boxes on the central and top right end of the system), and the *Ground* block (striped blue box on the bottom right end of the system), while the *Fluid ports* block at the bottom provides the system with the information related to every fluid stream entering and exiting the tank. Two output blocks, h and T_f, provide signals concerning the enthalpy and temperature of the molten salts stored inside the tank.

The two *Boundary_pT* blocks provide the environmental boundary conditions to the objects they are interacting with, as well as the *Ground* block does, with the only difference that in this last case the influence is modulated by the action of soil.

The tank's top and bottom surfaces are modeled as a series of thermal resistances (*ThResistor* blocks), each one related to one of the different layers these elements are composed of. In particular, the top side is divided into a metallic wall and an insulator, while the bottom side features an additional layer corresponding to the concrete basement. The lateral surface, instead, is described by an additional sub-model called *PipeWall*, able to take into account the cylindrical shape of the component and analyze conductive heat transfer phenomena both radially and axially. Similarly to the top side, wall

and insulation layers are treated separately through two different *PipeWall* blocks.

Last but not least, the behavior of molten salts and air inside the tank is analyzed by the *StorageHeat* (and its extension *PartialStorage*) block (white and blue box), which receives the heat flux values from the top, side, and bottom face sub-models as inputs, as well as the values of mass flow rate and temperature of the fluid entering the system, and combines this information in order to define, among many other parameters, the temperature evolution of molten salts.

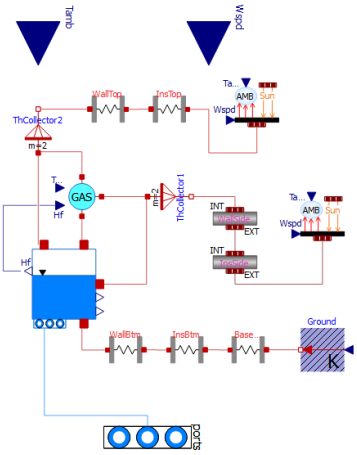

Figure 3.4: *Storage0D* model

3.1.2 Receiver

The receiver model aims at evaluating the heat gained by the heat transfer fluid (HTF), the heat losses from the receiver tube, and, consequently, the thermal efficiency. The model considers the fluid, the tube wall, the annulus (either evacuated or not), and the glass envelope. Moreover, it takes into account the effects of the secondary reflector on the radiation delivered to the receiver and the convective heat losses occurring from the glass outer surface. It has to be noted that this component could be omitted. Figure 3.5 shows a sketch of a typical receiver cross section.

The receiver tube is discretized along the axial direction into multiple sub-volumes, while only an elemental azimuthal discretization is applied, which divides the whole system into a top and a bottom side. This is performed because, while the bottom side directly faces the solar reflector field and receives the majority of intercepted solar rays, the top side is only affected by the minor share of radiation intercepted by the secondary reflector, an element that could potentially not be present at all.

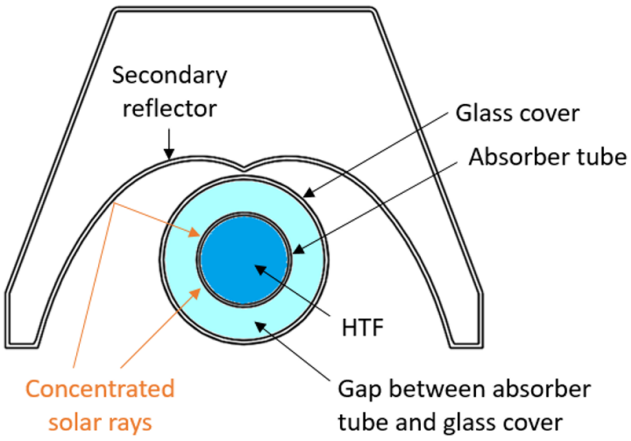

Figure 3.5: Receiver tube scheme [5]

Figure 3.6 shows all the heat transfer mechanisms taken into account in the model, which include:

- Heat convection between the wall and the HTF;
- Axial and radial heat conduction through the solid regions;
- Convective and radiative heat losses towards the external ambient;
- The azimuthal conduction is neglected.

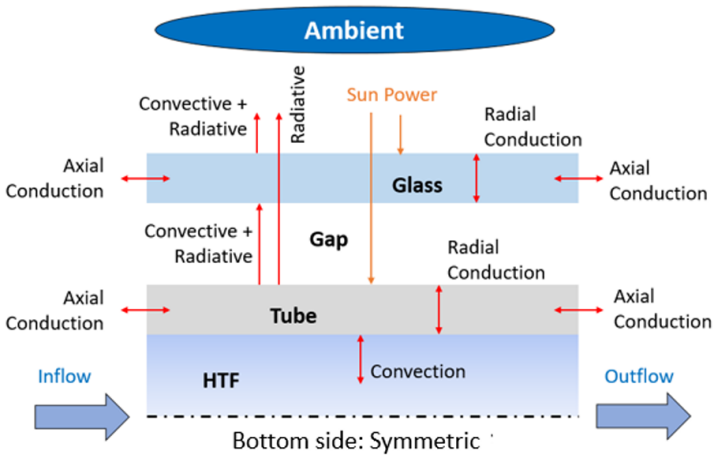

Figure 3.6: Receiver tube heat transfer mechanisms scheme [5]

As done for the storage system, the following Subsections will provide a short description of the OpenModelica models composing the LFR system.

ReceiverTube

This model is dedicated to the resolution of the mass, momentum, and energy balance inside the Linear Fresnel receiver, the axial and radial conduction in the metallic tube and the glass cover, as well as the convective and radiative heat transfer in the radial direction, eventually determining the heat losses characterizing the medium flowing inside this component. It exploits a multidimensional discretization in order to provide a more accurate description of the receiver tube:

- Azimuthal discretization: the component is azimuthally subdivided into two halves, a lower one on which is directly targeted by the radiation reflected by the mirror field, and an upper one that in the considered case is exclusively interested by losses due to the absence of a secondary reflector. A separation between the two volumes allows a more reliable evaluation of parameters.

- Axial discretization: the component is split into multiple sub-volumes along its axial direction, each one analyzed independently but able to communicate with the adjacent ones. This solution is adopted in order to describe the evolution of properties like temperature and losses as the axial coordinate changes.

Figure 3.7 displays the *ReceiverTube* Open Modelica model, in which the azimuthal discretization is immediately recognizable: the upper and lower halves, indeed, are exactly composed of the same blocks, but interact with different environmental conditions defined by the *AmbientBoundary_pT* component, which has already been encountered in the previous Sections. These two sides are modeled by two *PipeWall* blocks simulating the tube (internal element) and the glass layer (external element), and an additional *Annulus* block in between is dedicated to describing the heat transfer mechanisms between these two layers. The common central element *PipeFluid*, instead, models the behavior of molten salts flowing inside the receiver, provided the values of radiation and losses defined inside the outer Modelica layers. Every sub-volume into which the receiver is divided is virtually modeled by a system of equations defining this structure.

LinearCollector

This model provides the value of the solar power incident on the receiver as a function of DNI (Direct Normal Irradiation). The required data, provided in Appendix A, include the number of parallel mirror lines and their length, the collector azimuth and tilt angle, mirrors' optical properties, longitudinal and transversal IAM (Incident Angle Modifier), shadow and end-line efficiencies.

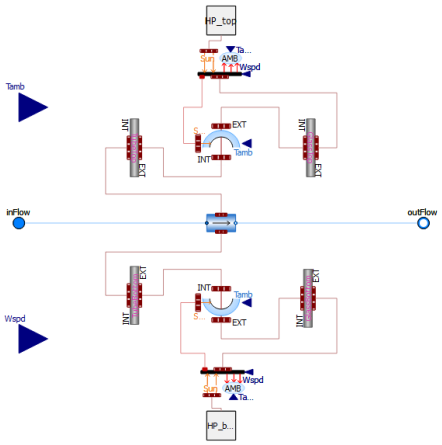

Figure 3.7: *ReceiverTube* model

LinearSystem

Figure 3.8 describes the model used to simulate the behavior of the entire Linear Fresnel mirror field and receiver system. What this block does is to allow the communication between *ReceiverTube* and *LinearCollector* and provide the results emerging from such interaction.

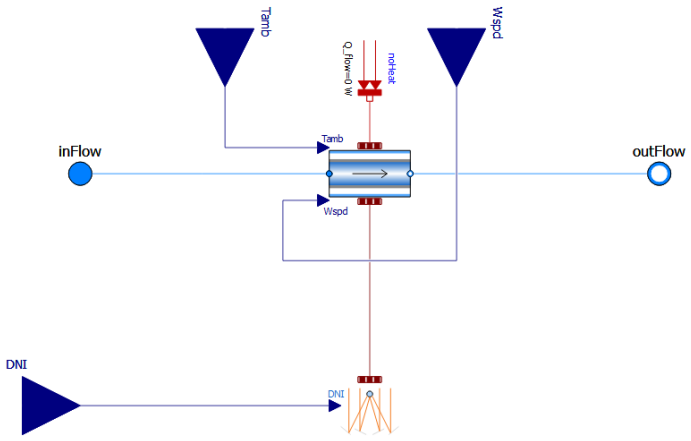

Figure 3.8: *LinearSystem* Fresnel receiver and collector model

In particular, the collectors are modeled by the component at the bottom (*LinearCollector*), which receives the value of DNI as input and computes the correspondent heat flux directed towards the lower side of the receiver block, represented at the center. The upper side is instead connected to a *FixedHeatFlow* block that imposes a defined value of power acting over this half receiver, in this case set to 0 W due to the already mentioned absence

of a secondary reflector. *ReceiverTube* also interacts with *Tamb* and *Wspd* input block, respectively providing the values of ambient temperature and wind speed to the model, which uses them to compute the evolution of different parameters related to the molten salts flowing inside, whose initial properties are provided by the *inFlow* block. The conditions of the medium at the receiver's outlet are then stored into the *outFlow* element in order to be forwarded to the next component.

3.2 Simplified model

This section provides an overview of the different simplified component models that have been explored in order to decrease their computational complexity, a feature that can be identified in the number of variables and equations needed to represent the component and the computation time of such mathematical system.

Despite the numerous interacting elements making up the Partanna CSP plant model, only two have been taken into account: thermal storage and receiver. This is justified by the fact that these two sub-systems are the most complex ones of the entire plant, and are modeled by a number of equations that results up to three orders of magnitude greater than the other elements. Consequently, a potential enhancement to these components would determine a more significant reduction in the macro-system overall computation times. Results will be provided and discussed in Section 3.3.

3.2.1 Thermal storage

Several models have been developed to reduce the complexity of heat storage tanks. For what concerns this component, the target with which the definition of alternative models has been approached was maintaining the molten salts temperature as close as possible to its original values, trying to reduce the complexity and number of equations needed to track other parameters of minor importance, and, possibly, even neglecting them.

Gas model removal

This version involves the complete deletion of every *Storage0D* sub-model dedicated to the simulation of the air volume enclosed between the molten salts free-surface and the tank's lid. Many are the factors suggesting that the convective heat transfer phenomena between the air and molten salts are expected to be limited:

- Reduced gas turbulence inside the tank;
- Extreme disparity between the densities of the two mediums (around 7 orders of magnitude);

- Limited temperature difference between the air inside the tank and the molten salts.

Assuming a comparable volume occupied by the air and the molten salts, in spite of the similarity between the specific heat capacities, such discrepancy in densities makes the amount of power transferable inside the salts much greater than the losses the air can generate. After the removal of gas-related components, then, medium temperature fluctuations are expected to be negligible.

The only heat transfer mechanism able to cause energy losses to the molten salts is in this case radiation between the medium and the tank's dry walls, which should in any case be limited due to an expected temperature similarity between these two bodies.

Figure 3.9 represents the *Storage0D* simplified version described so far.

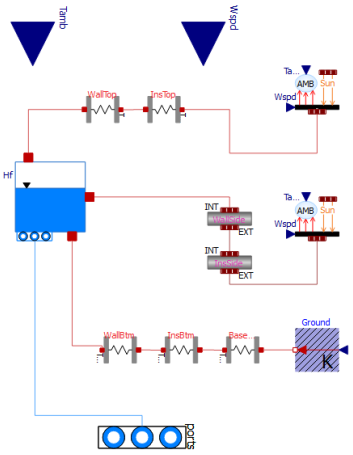

Figure 3.9: *Storage0D* model - Gas removal version

Wall model removal

An alternative version explores the possibility of completely removing the metallic walls separating the medium stored inside the tank from the insulation layer. This component, indeed, is characterized by high thermal conductivity and reduced thickness, so the thermal resistance R_λ associated with it is expected to be limited. The conductive heat flux q transferred in steady state conditions can be described by the following equation [7]:

$$q = \frac{\lambda \cdot A}{\Delta x} \cdot (t_1 - t_2) = \frac{\Delta t}{R_\lambda} \tag{3.1}$$

This implies that, for a given heat flux, the lower the thermal resistance value, the smaller will be the temperature difference between the two sides of the body, which in this case would result virtually transparent from a thermal point of view. It must be noted how the removal of this component could potentially have a significant influence on transients, which will have to be analyzed.

An important aspect to take into account is how the erased wall thickness has to be managed at this point, since it can be incorporated to the inner diameter, extending the volume occupied by molten salts, or alternatively added to the inner insulator diameter, increasing the portion of space occupied by this layer. What was decided to do was substituting the wall with other insulator, so the geometrical dimensions of the body do not undergo variations. After the removal, though, since wall and insulator are characterized by very different values of density, thermal conductivity, and specific heat, the tank's thermal response would end up being altered. Thus, several adjustments needed to be implemented:

- Density: Since the wall gets substituted by additional insulator, the total mass of the layer decreases, and this may lead to significant differences in the material's thermal response. Consequently, PyrogelIXT density has to be adjusted;

- Thermal conductivity: The new thermal conductivity is lower than the original, so it has to be substituted by an average value weighted on the two layers thickness;

- Specific heat: Similarly to thermal conductivity, specific heat has to be adjusted by implementing a weighted average.

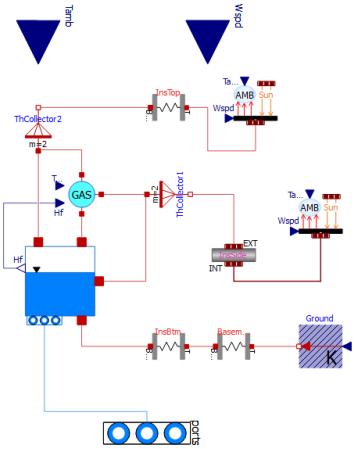

Figure 3.10: *Storage0D* model - Wall removal version

Figure 3.10 represents the *Storage0D* simplified version described so far. It can be noted how, while the *GasModel* block has been restored, the thermal resistances modeling every layer making up the top, side, and bottom tank surfaces have been reduced to a single one only representing the insulator. The block simulating the effect of the basement, instead, has been maintained.

Insulator temperature linearization

In order to make the system of equations easier to solve, an alternative way of reducing the computational effort is to consider the insulator layer as "thin". The implementation of the thin-wall approximation allows the system to consider the insulator thermal conductivity as independent from temperature, which causes the temperature evolution along the radial dimension to be modeled as linear. This would hopefully make calculations less complex, so a quicker system resolution is expected.

This simplification did not require any alteration of the code, but simply consisted in the activation of the thin-wall option in the insulator *PipeWall* block. It has to be noted that, for what concerns the side wall, this option has always been on because of its reduced thickness, which is in the order of magnitude of 1 mm.

On the contrary, the *ThResistor* blocks modeling the top and bottom faces of the tank do not make use of a thin-wall option.

Thermal resistances and pipe walls merge

This version extends the solution described in the *Wall model removal* version by synthesizing the characterization of the tank's layers to a single block per side.

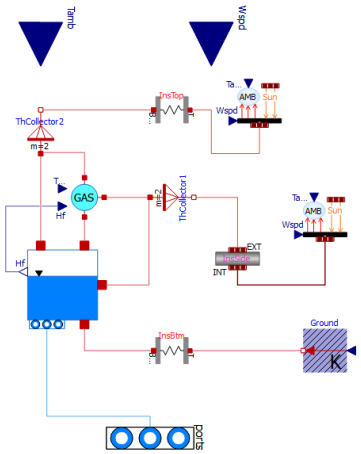

Figure 3.11: *Storage0D* model - Merged layers version

The only difference between Figure 3.11 and 3.10 is related to the bottom side, where three different layers have been merged, namely the metallic wall, the insulator, and the concrete basement. A weighted average has been used to adjust density, thermal conductivity, and specific heat, with the aim of aligning the behavior under steady state conditions, but a coherent evolution of parameters during transients has to be verified.

Adiabatic surfaces

Elaborating the outcomes of the previous simplified models, it has been proved how tank losses do not have an important impact on system performances, so the possibility of substituting the storage top, side, and bottom faces with adiabatic surfaces has been explored. Figure 3.12 shows how the *ThResistor* and *PipeWall* blocks modeling the tank's structure have all been substituted by *FixedHeatFlow* components, already employed inside the LFR model *LinearSystem* in Subsection 3.1.2, which imposes a constant heat flow acting on the element it gets connected to. Here the power has been set to 0 W on all three sides, defining in this way an adiabatic condition which importantly simplifies the system of equations from a computational point of view.

An interesting feature characterizing this version is its independence from wind speed: there is no more convection acting on the walls, indeed, so this parameter results irrelevant for what concerns the behavior of the tank. On the other hand, ambient temperature still results a factor due to its relationship with the *GasModel* block.

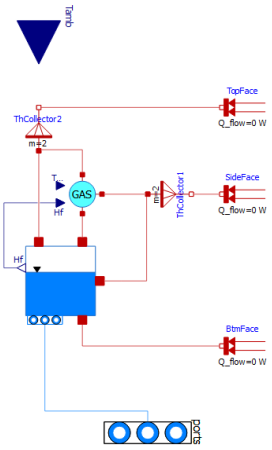

Figure 3.12: *Storage0D* model - Adiabatic walls version

In this way, it can be obtained what can be considered a limit model, where simplification of the tank is brought to the maximum. By implementing this type of solution, the losses generated by the interaction with the

top, lateral, and bottom surfaces are taken to zero.

Final model

In order to minimize the number of equations needed to model the storage system, an additional model was defined by combining together the most promising features of the alternatives examined so far. More specifically, with the intention of privileging the characterization of the medium's properties, the interaction of the tank with the external environment has been completely neglected, and its insulating layers substituted with adiabatic surfaces, in order to reduce as much as possible the number of equations needed to describe those elements. Moreover, the blocks modeling the air between the molten salts free surface and the tank's lid have been removed, as well as the ones dedicated to its interface with the external environment. In this configuration, the system results independent from both wind speed and ambient temperature values. On the whole, this final model is a combination of the *Adiabatic walls* and the *Gas removal* versions.

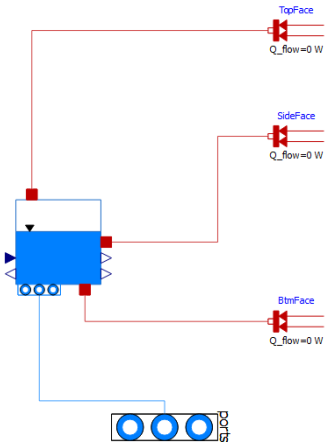

Figure 3.13: *Storage0D* model - Final version

Figure 3.13 presents a clear and intuitive image of the level of synthesis reached in the system's model, which gives priority to the characterization of the main parameters related to molten salts, essential in the definition of the whole CSP plant performances, while most of the other indicators are completely ignored.

3.2.2 Receiver

The simplified models targeting the receiver revolve around the possibility of reducing the degree of discretization used in its two characteristic dimensions: axial and azimuthal. It has to be noted, indeed, that the number

of equations needed to define a component is linearly proportional to the number of elements into which it is split, so acting on discretization levels could potentially lead to substantial computational load reductions.

This time, due to the considerable impact of heat losses on the receiver's performance, no simplification strategy was implemented for the structure and properties of the component.

Azimuthal discretization removal

This model has the objective to eliminate the receiver's differentiation between an upper and a lower side, and consider the component as a single entity. Despite the two halves being characterized by very different heat fluxes, the differences concerning the receiver and medium physical parameters should be limited, so results are expected not to worsen too much from the original version.

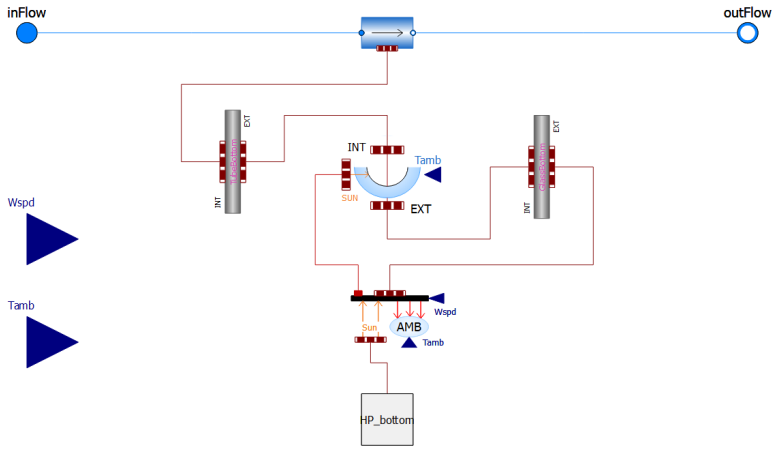

Figure 3.14: *ReceiverTube* model - Azimuthally simplified version

The component that has been primarily addressed is the *ReceiverTube* model, where, initially, the pipe fraction parameter *fp*, describing the angular fraction considered by each discretization, was set to 0.5 either for the upper and lower half *Annulus* and *PipeWall* elements. Instead of increasing *fp* to 1 on one side, and reducing to 0 the other, which generated issues in terms of equation solvability, *ReceiverTube* upper components have been decided to be completely deleted and *fp* set to 1 in the remaining lower half. The resulting version of the model is displayed in Figure 3.14.

PipeFluid and *LinearFresnel* models were consequently adjusted to fit the reduced set of variables. In the first component, since the corresponding receiver side has been deleted, the top heat port *HP2* (see Figure 3.7) was removed, while in the second the same thing was performed for the fixed heat flow source block interacting with the upper half of the pipe, as can be

seen in Figure 3.15. *PipeFluid* and *AmbientBoundaryPT*'s surface areas, in addition, were adjusted from 50% to 100% of the element's surface, since components resulted no more split in two halves.

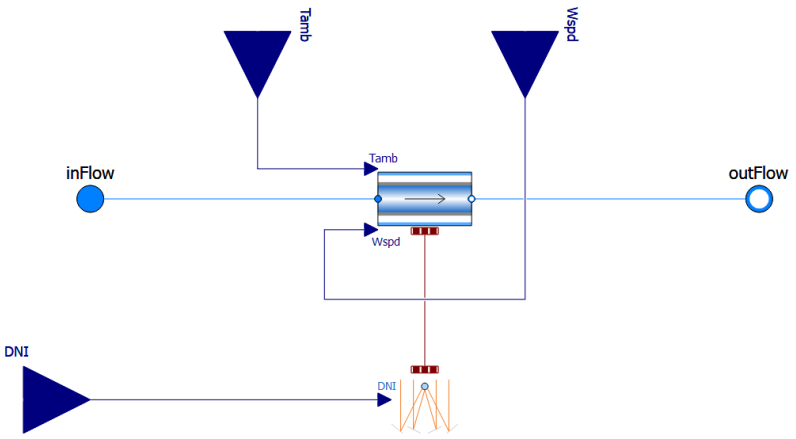

Figure 3.15: *LinearSystem* Fresnel receiver and collector model - Azimuthally simplified version

Axial discretization removal

In this alternative version, the receiver tube axial discretization process has not been applied, so that the sub-volumes the receiver is divided into, and then the number of equations needed to model the system, get minimized from an original amount of 9 different elements to a single one.

The component that has been addressed is the *LinearFresnel* model, where initially the number of nodes along the collector line was set to 10. The only thing that needed to be done was reducing this number to 2, so that the component gets modeled as a single volume enclosed between two detection points corresponding to the tube's inlet and outlet.

Differently from the alternative models seen so far, which pay a reduced accuracy in exchange for quicker run times, this particular simplified version will also produce a reduced amount of data for what concerns the axially-dependent parameters. Earlier, indeed, it was possible to get information about temperatures and heat fluxes as the axial coordinate varies, but the removal of axial discretization forces the model to introduce global indicators describing the system as a whole. Volume-related parameters, as a consequence, are characterized by a reduced ability to describe the model, and this is particularly true for fluid temperature, whose inlet and output values differ by hundreds of Kelvin and whose axial trend is not linear.

In the original model, a significant temperature level for every volume was defined by each couple of consecutive nodes' mean value, and this re-

sulted in 9 different elements able to provide a sufficiently accurate description. At this point, though, all that resulted available was a mere average between the input and outlet, not able to take into account the evolution of the system in between. A new definition of average fluid temperature was then conceived: instead of using multiple sub-systems and then calculating their average, what was exploited is a relationship that stems from the energy balance applied to a fluid flowing inside a tube, which provides a way to calculate how the section average fluid temperature T_m varies depending on the position x over the axis [4, p. 529]. The relationship is reported in the following equation:

$$T_m(x) = T_{m,0} + \frac{q''_s \cdot P}{m \cdot c_p} \cdot x, \tag{3.2}$$

where $T_{m,0}$ is the section average temperature at the receiver's inlet, q''_s the constant specific heat flux acting over the CERMET tube surface, and P the perimeter of the section.

This relationship was implemented into the Modelica *PipeFluid* script in order to find a representative temperature for the whole volume of molten salts flowing inside the receiver tube. After defining average fluid temperatures on multiple equally distributed sections all over the axis, these values have been averaged and a final representative temperature for the whole fluid inside the receiver was calculated. The logic followed in this case is substantially identical to the original case, with the exception that, in the face of a comparable outcome, the computational effort is reduced by almost 9 times. In order to result consistent with the original model, in addition, the HTF tube was divided into 9 different segments. In any case, this number can be increased to improve accuracy, minimally affecting computation time.

Final model

This last version combines the two previously analyzed models into a single one in order to simplify as much as possible the LFR model, minimizing the number of equations needed to describe its behavior.

3.3 Stand-alone systems simulations and results

This section summarizes the most relevant results obtained from simulating the previously mentioned models in a Modelica environment. First, two separate stand-alone simulations of the thermal storage and the solar block have been performed over a 24 hours time span in order to characterize their

functioning and reliability. By doing so, the different simplified alternatives examined so far have been compared both in terms of accuracy and run time, and the best performing models have been implemented in the Open Modelica digital representation of the entire Partanna CSP plant, examined in Section 3.4.1.

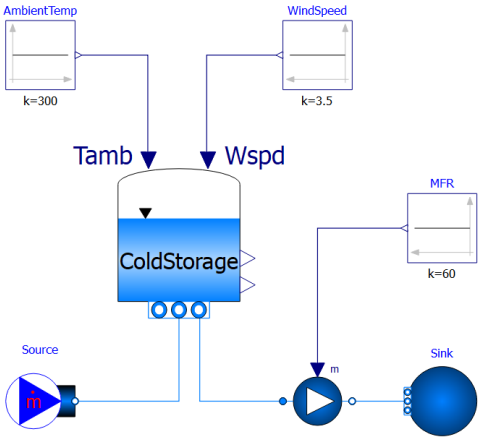

Figure 3.16: Heat storage stand-alone model

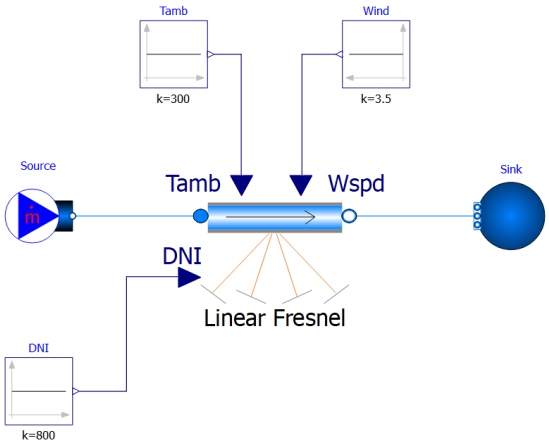

Figure 3.17: Solar block stand-alone model

In order to analyze their behavior, a stand-alone model of the thermal storage and the SB, consisting of the component itself, a mass flow source (*MassFlowSource_T*), and a sink (*Boundary_pT*), was created. This composition, represented in Figures 3.16 and 3.17, allows the two systems to be simulated independently, without the need to incorporate them into a more complex model representing the entire CSP plant.

The two models evaluate the thermal performances of the two components in steady-state conditions over 24 hours, which were considered sufficient to observe potential discrepancies building up in time. The ambient temperature, wind speed, and DNI input values are provided by *Constant* built-in Modelica block. It was decided, at least in this initial approach to the analysis, not to take into account realistic input data trends in order to be able to clearly assess the cause of possible inconsistencies affecting results. In case of a satisfying correspondence, a sensitivity analysis will be implemented to compare results under transient conditions.

The table below describes the Open Modelica daily simulation setup for the general 24 hours considered.

Property	Value
Start time [s]	0
Stop time [s]	86 400
Number of intervals	500
Integration method	dassl
Tolerance	10^{-6}

Table 3.1: Daily simulation setup (general day)

3.3.1 Thermal storage

The first model to be analyzed is the cold thermal storage (HT results have been omitted instead). Referring to Figure 3.16, the input values used have been the following:

- Ambient temperature: 300 K;
- Wind speed: 3.5 m/s;
- Inlet and outlet mass flow rate: 60 kg/s;
- Molten salts initial temperature inside the tank: 563 K;
- Molten salts inlet temperature: 563 K.

The model, consisting of 380 equations, took approximately 0.343 seconds to run, and the most significant results obtained from the simulation are provided below.

Molten salts temperature, defined in Figure 3.18, due to the heat losses experienced by the tank, seems to drop by a few tenths of a Kelvin in the first hours, and then stabilize to an approximately fixed value. This reduction is

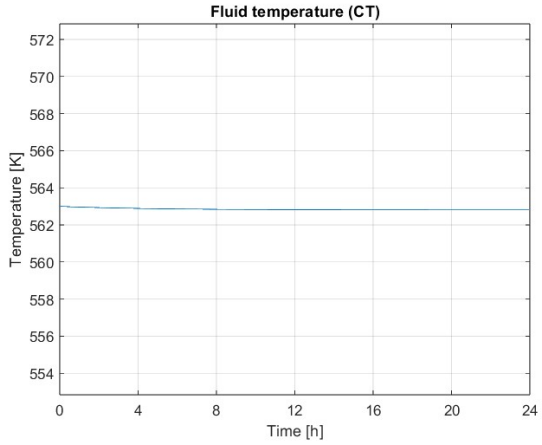

Figure 3.18: Molten salts temperature - Original cold storage

totally negligible if compared to the order of magnitude characterizing temperature values, and hints at the fact that heat losses are probably negligible when compared to the total amount of energy stored inside the medium.

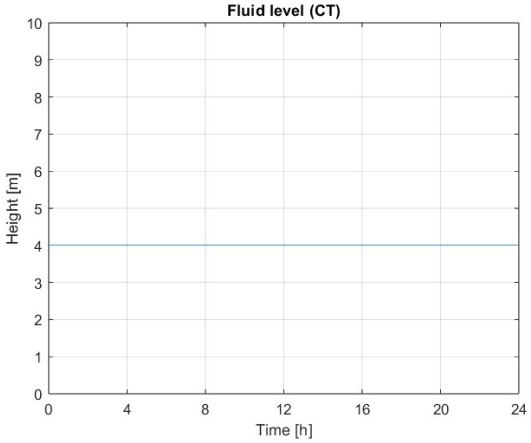

Figure 3.19: Molten salts level - Original cold storage

The level of fluid inside the thermal storage (Figure 3.19) does not go under any fluctuation, since the inlet and outlet mass flow rates coincide, but also no substantial temperature variation occurs, so the density and, consequently, the volume stay the same.

A quick calculation to corroborate the intuition concerning the limited importance of losses in this model can be made here. Starting from an average value of $1.76 \cdot 10^4$ W for total heat losses, provided by Figure 3.20, the energy associated with the volume of molten salts stored inside the tank [8] is given by:

$$Q_{ms} = m \cdot c_p \cdot (T_1 - T_0) = \rho \cdot h \cdot \frac{D^2 \cdot \pi}{4} \cdot c_p \cdot \Delta T \tag{3.3}$$

where m is the medium mass, c_p the specific heat capacity, ρ the volumetric density, h the height level, D the diameter, T_1 the temperature of molten salts, and T_0 the ambient temperature. The data needed to perform this calculation can be found in Tables A.2 and B.1. This formula provides a total energy of $3.97 \cdot 10^{11}$ J stored by the medium initially stored inside the tank. On the other hand, every second an amount of $1.76 \cdot 10^4$ J is lost by convection and irradiation. From this rule-of-thumb comparison, it is evident how losses result 7 orders of magnitude lower than the amount of available energy, not taking into account the fact that new hot fluid is continuously injected into the tank.

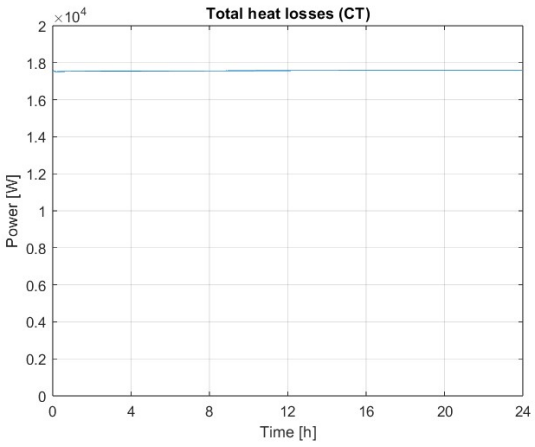

Figure 3.20: Total heat losses - Original cold storage

It can be said, then, that the portion of script dedicated to the definition of heat losses can probably be neglected without incurring relevant consequences.

Now that the original model has been analyzed, a description of the results generated from the stand-alone models implementing the *Storage0D* simplified alternatives will be provided.

Gas removal

In this version, the major parameters result to be substantially coincident, with the exception of gas-related losses, zeroed by the elimination of the *GasModel* block, but in any case characterized by a very limited importance if compared to the whole amount of energy dispersed. Molten salts temperature and height are identical.

A huge improvement is detected on computation times, which get cut 0.079 s, 77.0% less than the original configuration. The number of equations, instead, drops from 380 to 294 (-22.6%).

Wall removal

In spite of the density, thermal conductivity, and specific heat adjustments performed on the thermal resistance and pipe wall blocks modeling the insulator, heat losses values get completely messed up. While the radiative share increases by 71%, the convective one decreases by 55%, combining for a -32% on total heat losses. This provides a hint that the model is not so effective in incorporating the effect of multiple surfaces in a single one. The reason behind that was found in a strict dependence of these parameters on the metallic wall temperature levels, of which even small discrepancies from the original values could turn into huge differences for what concerns Grashof, Reynolds, and Rayleigh numbers, directly related to heat losses.

In any case, this condition does not affect the medium's temperature and level, which stick to their original values.

Even if the overall number of equations needed to model the system increases by 1, run times drop by 50.1%, indicating that the simplification of the top, lateral, and bottom tank layers greatly impacts computational complexity.

Insulator temperature linearization

The activation of the "thin-wall" option allows to linearize some of the equations needed to calculate heat losses. While accuracy is not affected at all and the number of equations does not change, run times decrease by 44.0%.

This result reinforces the deduction made for the previous model: the characterization of heat losses probably makes up most of the computational complexity the compiling program needs to manage.

Thermal resistances and pipe walls merge

As expected, extending the "Wall removal" logic to the *ThResistor* block dedicated to the concrete basement ends up worsening heat losses values, but improving computation times. The total share of heat losses, indeed, decreases by 38%, 6% less than what was found in the other model, but the time needed to simulate the system is just 0.148 s, 56.8% lower than before. Molten salts temperature and level still coincide with the original values.

Adiabatic surfaces

Taking the considerations made so far to the extreme, a limit solution involving a complete removal of the tanks' surfaces has been explored. Despite losing all the information related to heat losses, the computational simplification obtained is huge: while the number of equations gets reduced to 194 (-48.9%), run times drop down to 0.077 s, corresponding to a 77.6% decrease from the original condition.

Once again, molten salts temperature and height are not affected.

Final model

This last version, which combines gas removal with adiabatic walls, provides accurate results for both fluid temperature and level, while the information regarding heat losses is completely lost. Computation times, on the other hand, are reduced to just a fraction of the original values by using this configuration, dropping from 0.343 s to just 0.024, corresponding to a 93.0% decrease. The number of equations needed to model such a system is now 105, 72.4% less than the standard version.

Given the results obtained either in terms of numerical and computational performance, this configuration has been selected to be implemented into the Partanna CSP plant model with the purpose of making an year-long simulation possible.

3.3.2 Dynamic analysis

In order to validate this final model, a dynamic analysis was performed to assess its behavior under transitory conditions. Throughout an entire year, after all, input values are subject to important variations, so evaluating how the component responds to mutable conditions proves crucial to consider results as reliable.

The two parameters considered in this evaluation are inlet mass flow rate and inlet temperature, each one analyzed under two different evolution trajectories: constant and step variation. The first has been used to determine the dependence of some specific variables on the input, while the second has the purpose of characterizing the model's capability to provide accurate results under transitory conditions. Only the most significant features will be complemented by figures.

Inlet mass flow rate

In this first analysis, the cold tank model has been evaluated under multiple scenarios distinguished by alternative inlet mass flow values and trends.

Initially, the system was simulated with five equally distanced mass flow rate levels, ranging from 52 to 68 kg/s, which have been kept constant

through the whole 24 hours. It was decided to use at most just an 8 kg/s step in order to avoid a tank overload or depletion before the 24 hours horizon. Other input parameters requested by the model are:

- Ambient temperature: 300 K;
- Wind speed: 3.5 m/s;
- Outlet mass flow rate: 60 kg/s;
- Inlet temperature: 563 K.

None of the five scenarios explored led to variations in the temperature of the medium, both in the original and final versions of the model. The only parameters to change in time, as expected, were molten salts level and volume.

After that, two additional input patterns were explored. More specifically, the inlet mass flow was maintained at a fixed rate of 60 kg/s for the first 4 hours, followed by a sudden step variation of +8 kg/s in the first case, and -8 kg/s in the second, which was maintained for the remaining 20 hours. A control scenario characterized by a constant inlet value of 60 kg/s was also defined to allow comparisons. Ambient temperature, wind speed, and outlet mass flow rate values were not modified.

Similarly to the previous case, molten salts temperature did not change in the three situations under examination.

Inlet temperature

This time, the cold tank model has been tested using different inlet temperature values and patterns.

Following the exact same procedure used before, the system was initially simulated under five equally distanced inlet temperature constant values, selected from a reasonable operative range and whose trends are reported in Figure 3.21. The other parameters are:

- Ambient temperature: 300 K;
- Wind speed: 3.5 m/s;
- Inlet and outlet mass flow rate: 60 kg/s.

As expected, simulations demonstrated how this parameter proves crucial in the definition of molten salts temperature inside the tank. Referring to Figure 3.22, after an initial steep variation, trends reach a plateau after around 18 hours, which is an information of crucial importance for what concerns the operations of the plant. Considering, for instance, a maximum

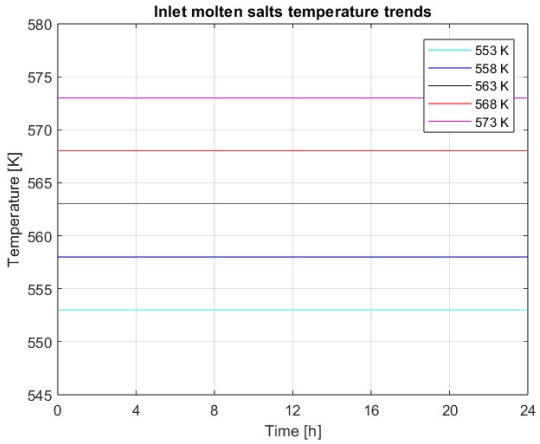

Figure 3.21: Constant inlet temperature trends

mass flow rate around 120 kg/s, twice as much the value used in the simulation, the medium stored inside the heat storage would reach a potentially dangerous temperature in no more than 10 hours if an excessively hot or cold molten salts flow is provided.

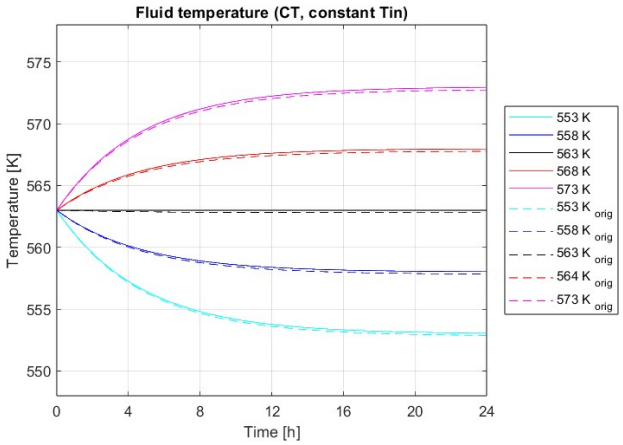

Figure 3.22: Medium temperature evolution under different constant inlet temperature conditions

The plot also provides a comparison between the trends obtained for the final model (continuous lines) and the original one (dashed lines), showing how the simplified alternative provides excellent results even in transients. The slight discrepancy characterizing molten salts temperatures can be explained by the enormous heat capacity difference existing between the medium and the wall or insulator materials (see Table 3.2). It appears that these layers have just a minimal influence on system thermodynamics. The

temperature difference between the two trends, equivalent to a few tenths of a Kelvin, is due to the distinct way heat losses are taken into account by the two models.

Property	Molten salts	Wall	Insulator
Specific heat capacity [J/kg/K]	1493	530	1046
Density [kg/m^3]	1903	8238	100
Volume [m^3]	$5.31 \cdot 10^2$	$1.13 \cdot 10^{-4}$	$5.03 \cdot 10^{-1}$
Heat capacity [J/K]	$1.51 \cdot 10^9$	$4.94 \cdot 10^2$	$5.26 \cdot 10^4$

Table 3.2: Heat capacity comparison

The same parameter was then evaluated under two different step function inlet temperature patterns. As displayed in Figure 3.23, a starting value of 563 K was adopted for the first 4 hours, followed by a jump (or drop) of 10 K, which was maintained until the end of the day.

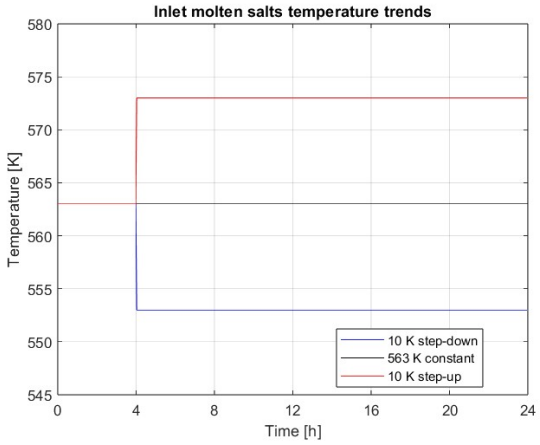

Figure 3.23: Step function inlet temperature trends

Results confirm what has been stated earlier, highlighting, in addition, a minimal latency in the medium's response. The outcomes are displayed in Figure 3.24.

3.3.3 Receiver

The second model to be simulated in a stand-alone configuration is the LFR system, mainly composed of a collector and a receiver. Referring to Figure 3.17, the input values used have been the following:

- Ambient temperature: 300 K;

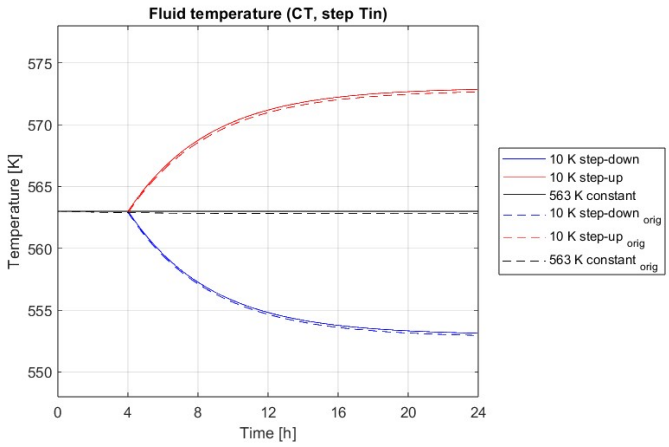

Figure 3.24: Medium temperature evolution under different step function inlet temperature conditions

- Wind speed: 3.5 m/s;
- Inlet and outlet mass flow rate: 60 kg/s;
- Molten salts initial temperature inside the tank: 563 K;
- Molten salts inlet temperature: 563 K;
- DNI: 800 W/m^2;
- IAM: 1.

The model, much more complex than the heat storage, consists of 2014 equations and took 0.456 seconds to be run. The most significant results obtained from the simulation are provided below and are all referred to a single solar loop.

The first element to be considered is the collector, which is in this case characterized by three different parameters: Q_{sol}, product of DNI and mirror area and representing the total heat flux to which the reflecting system is exposed to, Q_{rec}, corresponding to the share of power actually hitting the receiver tube after being deflected by the mirrors, and Q_{loss}, which represents the amount of heat dispersed due to optical losses, in this case around 29.6%.

Focusing on the receiver tube, simulations show how the fluid is under steady-state conditions, since none of the parameters describing it goes under variation in the 24 hours considered. In particular, temperature has a value of 563 K at the inlet, 984 at the outlet, with an average over the whole receiver's length of 785 K. It must be noted how, due to an excessive DNI to mass flow rate ratio, the fluid far exceeds the limit temperature of 833

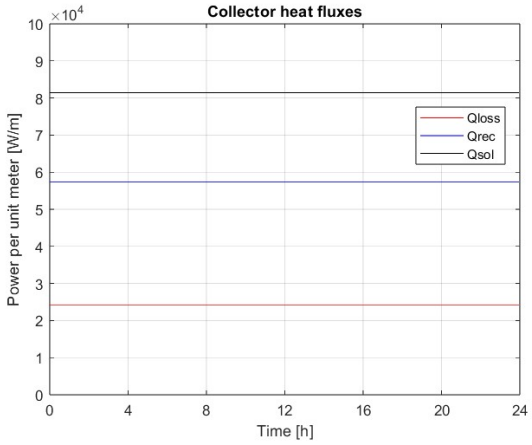

Figure 3.25: Collector heat fluxes - Original solar block

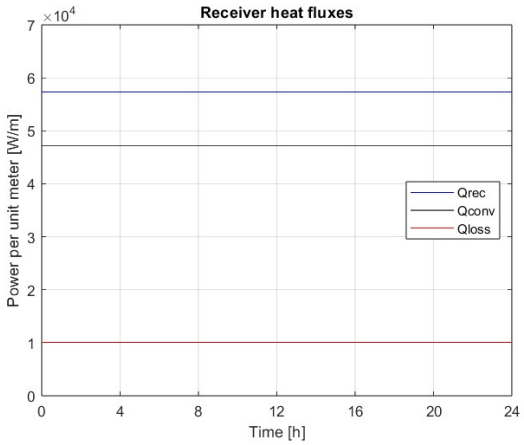

Figure 3.26: Receiver heat fluxes - Original solar block

K, over which degradation might be triggered. This is due to the absence of a mass flow rate regulation system, which will be introduced later on when the whole CSP plant is taken into account.

Figure 3.26 characterizes the component in terms of heat fluxes. While Q_{rec} represents the receiver's heat source, Q_{conv} constitutes the fraction of power actually reaching the molten salts and generating its temperature increase. Not all the power intercepted actually turns into useful heat, though, but some of it (Q_{loss}), in this case 17.6% of the availability, gets lost as the fluid heats up and approaches the output.

Figure 3.27, instead, explores the differences between the two sides into which the receiver is discretized. The lower half is characterized by a positive heat flux, meaning that the energy flow is directed towards the system and

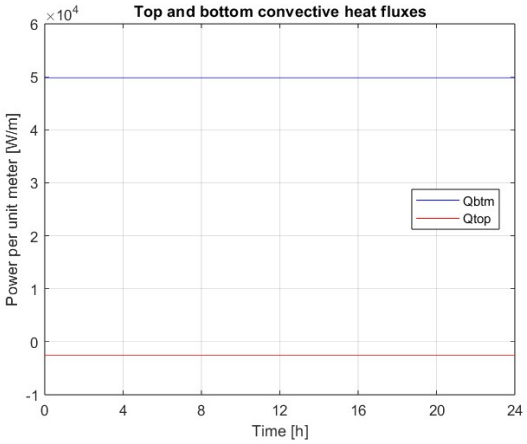

Figure 3.27: Receiver convective heat fluxes - Original solar block

positively contributes to its energy balance. The upper half, instead, is not directly exposed to the radiation reflected by the solar field, and ends up delivering power back to the environment, even if this amount is roughly one order of magnitude lower than the absorption on the lower end. This information confirms the absence of a secondary reflector. It must be noted how the values displayed are referred to the whole length of the receiver, which features increasing temperatures as the fluid gets closer to the outlet. Convective heat fluxes and losses, as a consequence, are not constant in space and evolve over the axial coordinate, as will be further explained on page 48.

The results generated by the three stand-alone models implementing *ReceiverTube* simplified alternatives will now be analyzed.

Azimuthal discretization removal

In this version, a direct comparison could not have been carried out due to the dissimilarity in the number of volumes the receiver was divided into, two in the original model and one in the simplified alternative. What has been decided to do, then, was grouping the indicators describing the two original halves into comprehensive values and comparing them with the ones characterizing the other model. This translated into averaging temperature levels and algebraically summing heat fluxes. No significant discrepancy emerged.

On the other hand, though, performances improved sensibly compared to the original case: a reduction to 1175 equations (-41.7%), indeed, has led to a computation time of 0.310 s, 32.0% less than the original value.

Axial discretization removal

This second model reduced the number of sub-volumes into which the receiver tube was split from 9 to 1, forcing the compiler to consider its 817.6 m as a single element. Due to the important energetic fluctuations occurring along the axial coordinate and the capability of the one-dimensional model to characterize molten salts with just a single temperature value, the difficulty results in properly defining temperature-dependent variables. This criticality emerged, in particular, in the definition of fluid properties.

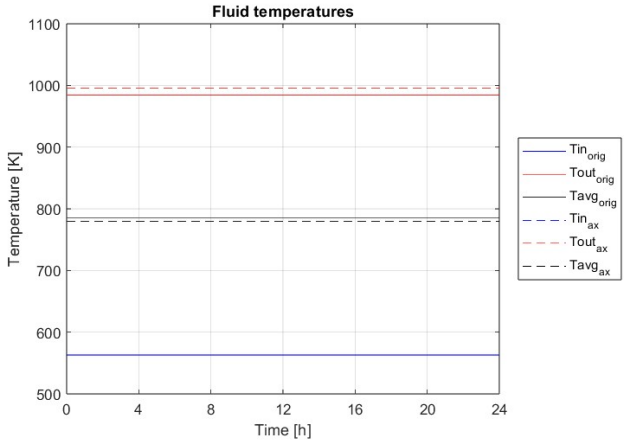

Figure 3.28: Receiver fluid temperatures comparison

As Figure 3.28 highlights, the average and outlet molten salts temperatures slightly differ between the two models. A lower average value, 779 K against the original 785, suggests a slower evolution of the parameter, followed by a sharper increase at the receiver's end which justifies a greater outlet temperature of 996 K, 12 more than before. These differences, though, are limited: if referred to the temperature range covered by the fluid in the original model, the average results just 1.4% lower, while the outlet value is 2.8% greater.

The reason behind these numbers can be found in Figure 3.29, which describes how this alternative model proves to be less sensitive to heat losses, 13.6% lower than their original counterpart. It follows that a greater convective power flux is able to reach molten salts and heat them up, justifying the increased temperature levels observed in the previous plot.

On the other hand, though, the removal of axial discretization guarantees huge performance improvements: 83.0% reduction in the number of equations, which drop to just 343, leading to a mere 0.052 s run time, 88.6% lower than originally. These results, given the scope of the project, make the slight reduction observed in accuracy an acceptable drawback.

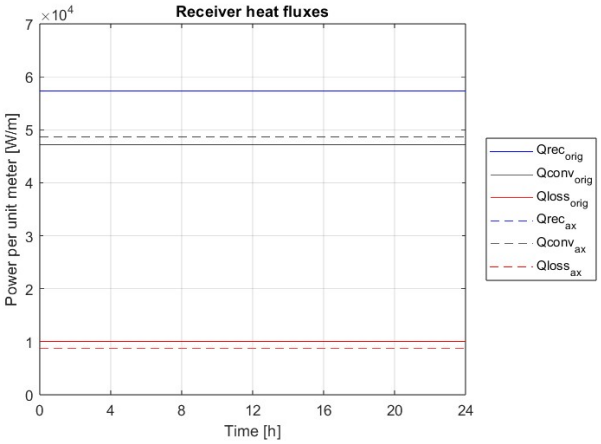

Figure 3.29: Receiver heat fluxes comparison

Spatial analysis

Before proceeding with the final and most synthetic *ReceiverTube* version, the focus will be briefly shifted on the evolution of parameters in space. As anticipated, indeed, in a steady-state regime temperatures and, consequently, heat fluxes, though constant in time, result to be dependent on the axial coordinate: while flowing inside the receiver tube, molten salts are exposed to solar radiation, which gradually heats them up as they approach the outlet.

Figure 3.30, in particular, highlights the relationship existing between the axial coordinate and the receiver tube heat fluxes. A comparison in the way they are modeled in the original, azimuthal, and axial simulations is also provided.

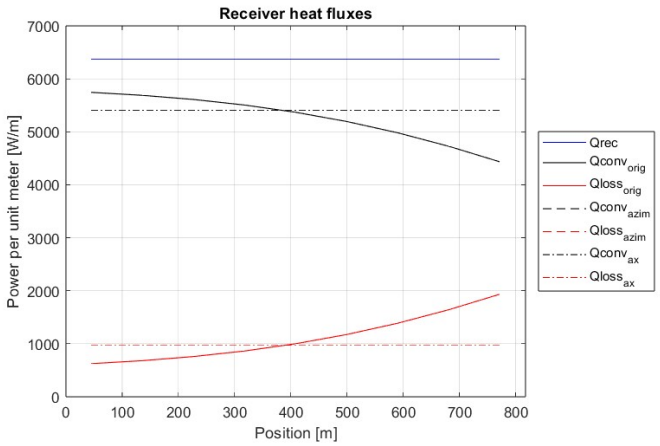

Figure 3.30: Space dependent receiver heat fluxes

It has to be noted how the values reported in Figure 3.26 are different from the ones provided in this representation, and this is due to the different "x" axis used. When plotting on time, the value of power refers to the heat flux exchanged by the whole receiver's length at that particular moment. When plotting on space, instead, the value is referred to the power flux characterizing that particular axial coordinate, assuming the receiver's inlet section as the origin.

The chart highlights how, while the power hitting the receiver is equally distributed, the other two heat fluxes follow different patterns depending on the model used: in the case of the original or azimuthally-simplified versions, losses gradually increase as the fluid travels the tube, causing convective heat fluxes to drop, but in the case of the axially-simplified model the trend is linear. This last trend is due to the absence of multiple detection points in correspondence of which parameters are evaluated. The receiver tube, indeed, is modeled by only 2 nodes enclosing a single volume, whose features are all computed at the average temperature defined by Equation 3.2. The other two models, instead, exploit 10 nodes which confine 9 different volumes, each one of which corresponds to a sub-system of equations that gets solved independently. This allows the model to obtain a distribution of points along the axis that can be used to create a spatial characterization of the system.

Molten salts temperature trends are represented in Figure 3.31, while the evolution of thermal efficiency is described by Figure 3.32.

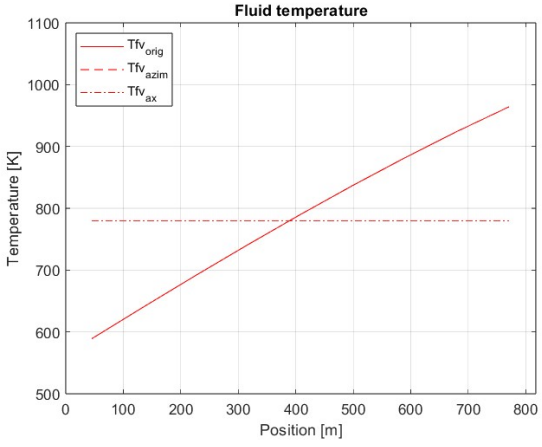

Figure 3.31: Space dependent receiver temperature

Final model

Now that the first two *ReceiverTube* alternatives have been examined and compared, a final version will be presented.

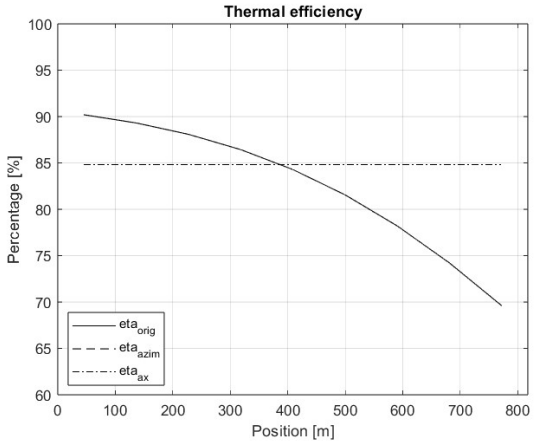

Figure 3.32: Space dependent receiver's thermal efficiency

This last model combines azimuthal and axial discretization removal to reduce as much as possible the LFR complexity, minimizing the number of equations needed in order to describe its behavior. Results proved to be substantially coincident with the ones obtained by the axially-simplified stand-alone system, even if computational performances further increased: the resolution of a system of 232 equations (-88.5% compared to the original version) took only 0.046 s, corresponding to 10.1% of the time needed initially.

3.4 Partanna CSP plant simulations and results

The aim of the Partanna CSP model is to predict the thermal-fluid-dynamic behavior of the entire solar loop, determining the energetic and economic performance of the system. Moreover, as described on page 18, the solar loop model can be exploited to test two different control strategies: *Integration* and *Antifreeze*.

Figure 3.33 displays the Open Modelica blocks scheme of the CSP plant in *Integration* mode. Starting from the CT, where they are stored at a temperature between 550 and 600 K, molten salts are sent to the SB through a pump. After that, the flow gets split in two: most of the mass flow rate is directed towards the solar field, but a minor fraction, modulated by a control block, is deviated to a GFH in order to guarantee thermal support to the LFR system. This regulation is operated by the *FlowController*, a PID-based mass flow rate controller that, acting on the valve opening, regulates the pressure drop in the heater branch. The two streams converge into the HT, where the medium is stored at high temperature, waiting for a signal from a second pump that directs it towards the PB, where, depending on

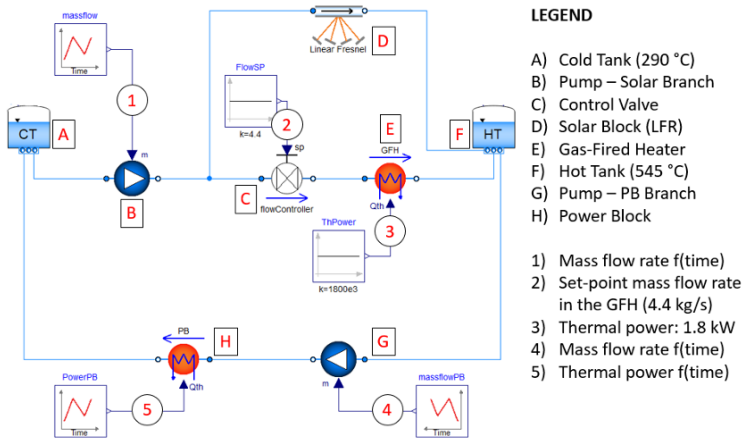

Figure 3.33: Partanna CSP plant Open Modelica model - *Integration* [5]

the load, part of its thermal power is removed. After being cooled down, molten salts return to the CT.

A different exploitation of the GFH branch is instead adopted in *Antifreeze* mode, where this stream is directly sent back to the CT. This is performed to prevent the cold medium from freezing overnight or when particularly unfavorable weather conditions occur. The alternative configuration is displayed in Figure 3.34.

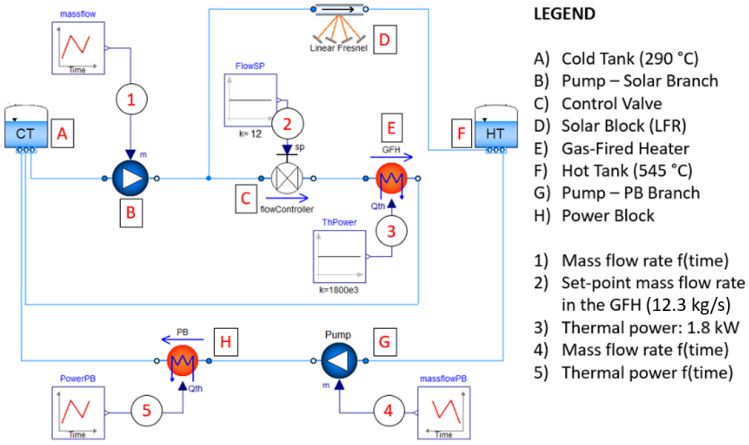

Figure 3.34: Partanna CSP plant Open Modelica model - *Antifreeze* [5]

3.4.1 Daily simulation

This subsection provides the results for both configurations of the solar loop, considering June 09, 2015, as the reference day. All the information

required by Open Modelica in the definition of the Partanna CSP model and materials properties can be found in Appendix A and B, while the setup is described in Table 3.3.

Daily input data trends like ambient temperature, wind speed, pumps mass flow rate, DNI, and power load have all been provided by FATA and are graphically represented in Appendix D, while IAM values can be found in Appendix C. A detail to be noted is that, for the sake of simplicity, the *Integration* configuration uses the same mass flow rate for both pumps, while in *Antifreeze* mode the PB pump is set to a value equal to $\dot{m}_{PB} = \dot{m}_{SB} - \dot{m}_{GFH}$.

Simulations have been performed with both original and simplified alternatives, whose results will be analyzed and compared to assess accuracy and performance differences. Only the most significant indicators will be taken into account.

Property	Value
Start time [s]	13 737 600
Stop time [s]	13 824 000
Interval [s]	600
Integration method	dassl
Tolerance	10^{-6}

Table 3.3: Daily simulation setup (09-06-2015)

Integration configuration

In this first simulation, the fluid level inside the two tanks undergoes small variations during the 24 hours considered. The simplified model, whose values are specified inside the legend with the subscript "alt", slightly differs from the original for what concerns results, showing an absolute relative difference [1] of 2.5% in the case of CT, and 3.9% for the HT, which corresponds to less than a centimeter in both cases, though.

Similarly, temperatures show differences around 2.5% for the CT fluid ($\pm$1 K), and 2.7% for one stored inside the HT ($\pm$3 K). For what concerns molten salts at the receiver's output, the average relative discrepancy was assessed around 2.6%, corresponding to a difference of $\pm$8 K. All in all, these values do not seem to particularly affect model accuracy, since, as clearly visible from the charts, indicators seem to follow pretty accurately the original trend.

[1] Relative differences are referred to the maximum variation in values registered inside the 24 hours.

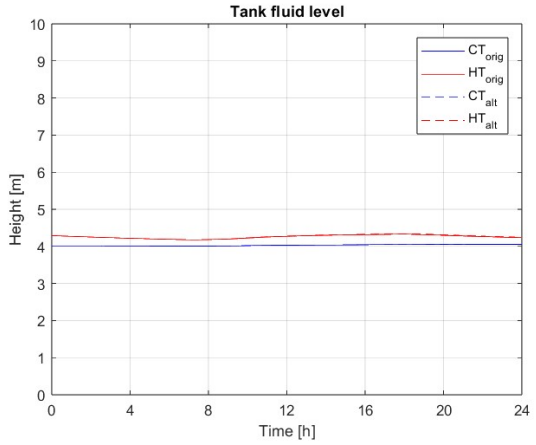

Figure 3.35: Daily tank's medium levels - Integration

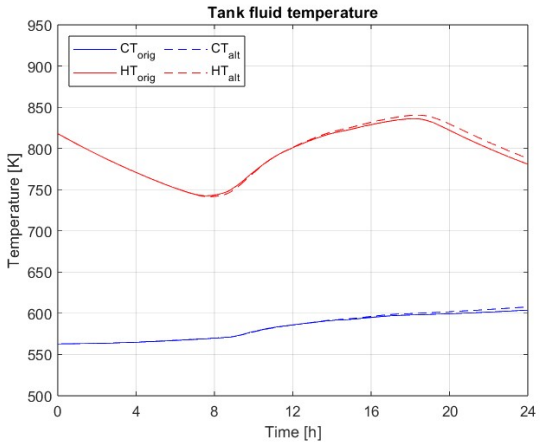

Figure 3.36: Daily tank's medium temperatures - Integration

Figure 3.38 shows how mass flow rates change in time through the SB and GFH branches. This configuration, in particular, provides an almost constant flow of 4.4 kg/s to the fossil back-up heater, adapting instead the solar field share depending on environmental conditions (DNI in particular) in order to prevent the fluid inside the receiver from reaching excessively high or low temperatures.

The power generated by the plant along the 24 hours is represented instead in Figure 3.39, and takes into account both the shares produced by the GFH and the SB.

In the original model, the daily thermal energy yield resulted to be 326.1 MWh_{th}, while the simplified alternative generated 327.9 MWh_{th}, which, considering a thermal-to-electrical energy conversion ratio of 0.4, respec-

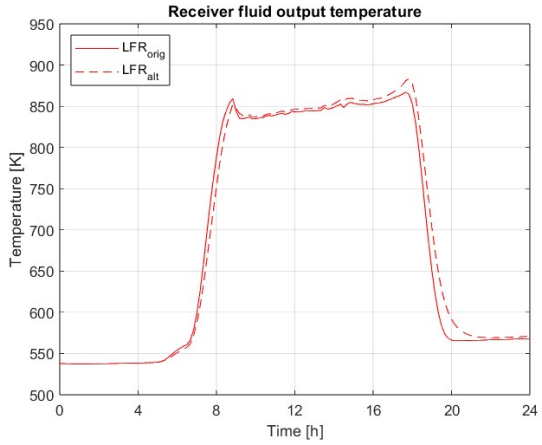

Figure 3.37: Daily receiver outlet temperature - Integration

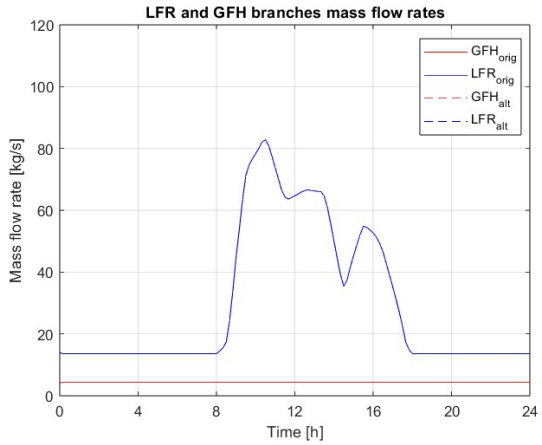

Figure 3.38: Daily SB and GFH mass flow rate - Integration

tively correspond to 130.4 and 131.2 MWh_{el}. Breaking down these numbers, both versions registered a GFH generation of 43.2 MWh_{th}, while a little difference emerged in the solar-powered branch, whose production resulted to be 282.9 MWh_{th} in the original configuration, and 284.7 in the simplified one. Heat losses do not seem to have an impact over these values since the average medium temperature inside the receiver is substantially coincident at 636 K. This difference can instead be explained by the slightly higher average fluid temperature at the receiver's end recorded in the second simulation (694 K, against the original 690 K). Such a discrepancy, around just 0.6% of the total energy yield, can be considered totally acceptable given the improvements in computational performances ensured by the last model. The original set of 2771 equations has been reduced to a system of

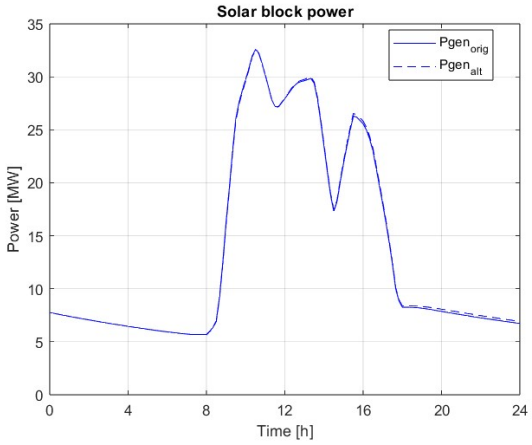

Figure 3.39: Daily power generation - Integration

just 443, which took just 1.85 s to simulate, instead of the 23.77 originally required.

Antifreeze configuration

The operation in *Antifreeze* mode produces slightly different results, but it can be said that the simplified model does a really good job here too.

Fluid level discrepancies were found to be even smaller under this circumstance: 0.1% for the CT, and 0.7% for the HT, reflecting not even a difference of 1 cm.

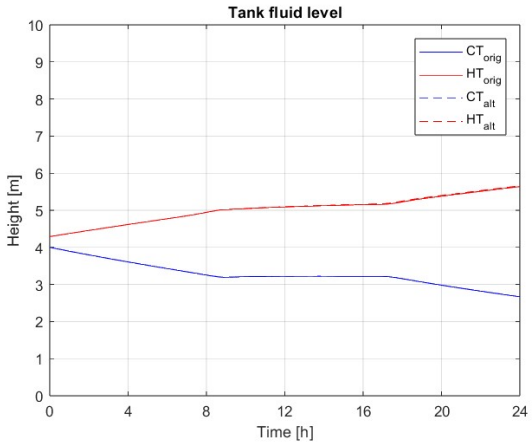

Figure 3.40: Daily tank's medium levels - Antifreeze

Temperatures, instead, present differences close to the ones seen earlier: 2.4% inside the CT (±1 K), 3.3% in the HT (±3 K), and 3.1% for the fluid

at the receiver's output (±12 K). Even under this configuration, results can be considered satisfactory due to a good overall adherence in terms of both dynamic response and numerical values.

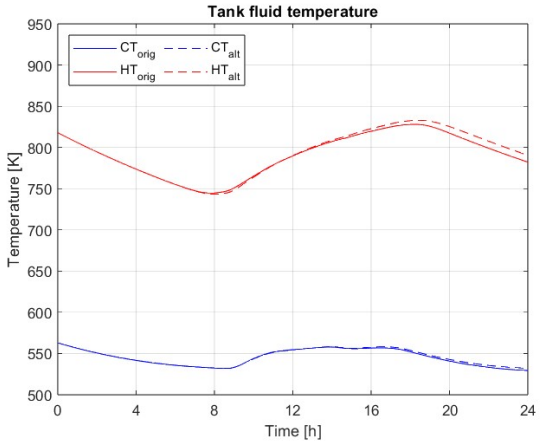

Figure 3.41: Daily tank's medium temperatures - Antifreeze

On the other hand, the mass flow rates measured inside the two branches show important differences compared to the previous configuration. A much greater stream, characterized by a minimum of 5.6 kg/s and a maximum of 12.3, is directed towards the GFH and then bypassed to the CT, ensuring in this way higher minimum temperatures, but at the same time lower energy levels inside the HT. Since the SB pump is characterized by the same mass flow rate pattern seen before, the one right at the beginning of the PB ends up pushing a significantly minor amount of molten salts, which will end up having an impact on the energy yield.

The daily thermal energy production resulted to be 203.5 MWh_{th} in the original model, and 204.3 in the simplified one, corresponding to 81.4 and 81.7 MWh_{el}. The share of energy produced by the GFH system adds up to the same 43.2 MWh_{th} registered before, but significantly increased in relative terms, rising from 13.2% to 21.2%, at the expense of the SB generation, respectively dropping to 160.3 and 161.1 MWh_{th}.

As anticipated, these values result significantly lower than the yields obtained with the *Integration* configuration (-43.3%), and this is due to two main reasons: colder fluid at the receiver's end and lower mass flow rate directed towards the power block. The average temperatures characterizing molten salts at the receiver tube exit are 678 K for the original model and 684 K for its counterpart, roughly 10 K colder than the values found in *Integration* mode, which may be found surprising. Providing a lower mass flow rate to a system subject to the same irradiance should cause the medium to reach higher temperatures, but as can be observed by comparing Figures 3.37 and 3.42, the *Antifreeze* scenario features higher peaks, but, more

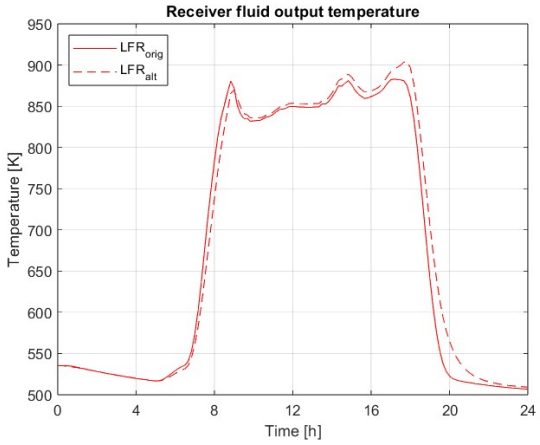

Figure 3.42: Daily receiver outlet temperature - Antifreeze

importantly, lower troughs, which characterize the fluid for much longer periods of time, decreasing mean values. Lower mass flow rates, on the other hand, determine minor power fluxes that, integrated in time, cause the daily energy yield to be smaller.

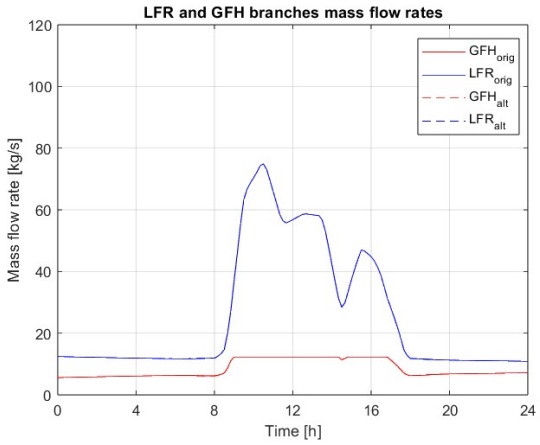

Figure 3.43: Daily SB and GFH mass flow rate - Antifreeze

In any case, a mere 0.4% difference in energy levels is completely acceptable when computational performances are taken into account. The number of equations making up the model, originally 2776, has been reduced to 448, which has translated to a 93.2% cut in run times, dropped from 29.01 to 1.96 s.

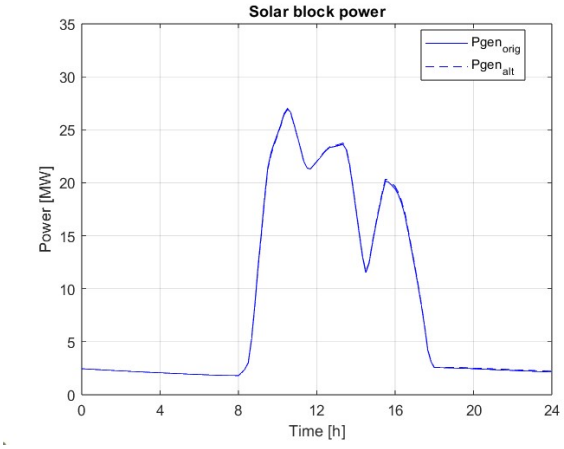

Figure 3.44: Daily power generation - Antifreeze

3.4.2 Yearly simulation

This second subsection provides the results obtained for both configurations in a whole typical year, which was defined using the site's related data retrieved from "PVGIS" [9] starting from the exact location coordinates. The solar radiation database used is "PVGIS-SARAH3", and the considered time range spans from 2005 to 2023. All the information required by Open Modelica in the definition of the Partanna CSP model and materials properties can be found in Appendix A and B, while the setup is described in Table 3.4. Due to the much greater amount of time that needed to be considered, the time step value has been increased from 10 minutes to 1 hour, corresponding to a density of 8760 values per parameter.

Property	Value
Start time [s]	0
Stop time [s]	31 536 000
Interval [s]	3600
Integration method	dassl
Tolerance	10^{-6}

Table 3.4: Yearly simulation setup (typical metereological year)

Yearly input data trends like ambient temperature, wind speed [2], and

[2] A first simulation attempt failed due to numerical issues in the occurrence of null wind speeds. In order to overcome the problem, those values (less than 10 timesteps in the whole dataset) have been substituted with a velocity of 0.1 m/s.

DNI obtained from "PVGIS" are graphically represented in Appendix E. Again, for the sake of simplicity, the *Integration* configuration uses the same mass flow rate for both pumps, while in *Antifreeze* mode the PB pump is set to a value equal to $\dot{m}_{PB} = \dot{m}_{SB} - \dot{m}_{GFH}$.

Simulations have been performed exclusively with simplified models.

Mass flow rate control system

Originally conceived to provide results over short transients, the two models, when run with datasets containing information about a whole year, end up aborting the simulation after just a few days, usually due to one of the two storage tanks overcoming their maximum or minimum fluid level allowed. A mass flow rate control system, able to operate a multi-parameter modulation of the two pumps, is completely absent indeed. Since the definition of a PID-based mass flow rate fine-tuning system results a relatively complex operation that goes out of the scope of this project, an alternative solution was found.

The first thing to be done was targeting the main parameters regulating the action of the two pumps, which were identified in the receiver's outlet fluid temperature and the tanks' fluid level.

In order to control the medium's temperature, a new Modelica block called *MFR_calculator* was created. It receives as input the values of CT fluid temperature, irradiance acting over the receiver's surface, and GFH-branch mass flow rate, and computes a suitable amount of fluid to send to the SB to keep the temperature of molten salts at the end of the receiver as close as possible to a target value of 818 K. The implemented function, achieved by implementing the energy equation to the thermal vector, is the following:

$$\dot{m}_{PB} - \dot{m}_{GFH} = max(\frac{\eta \cdot Q_{rec}}{c_p \cdot (T_{out} - T_{in})}, 18) \tag{3.4}$$

The parameters considered are the receiver's average thermal efficiency $\eta = 0.85$, the target outlet temperature $T_{out} = 818$ K, and the molten salts average specific heat $c_p = 1.5187 \cdot 10^3$ J/kg/K, while the GFH mass flow rate $\dot{m}_{GFH}$, the irradiance Q_{rec}, and the receiver's inlet temperature T_{in} are parameters acquired from external components making up the CSP model. What the algorithm does is to define the mass flow rate needed to get the fluid as close as possible to the target temperature, increasing it as the heat flux coming from the Sun gets higher. In case of limited irradiance values, though, it may happen that the flow has to be excessively reduced, with the risk of exposing molten salts to conductive and radiative losses for a prolonged period of time, a possibility that could cause it to exceed the

safety boundary of 543 K and start freezing. In order to avoid this dangerous condition, a minimum SB mass flow rate of 18 kg/s was imposed.

The second criticality was that, in spite of flow regulation, a possible excessive difference between the plant's generated power and the external load could verify and lead the two tanks to a possible depletion or overload of molten salts. A possible solution could be to differentiate mass flow rate signal patterns across the two pumps, increasing PB's pump activity when the load gets higher than the available power and vice-versa, but once again, without adequate control and regulation systems, the occurrence of level-related issues seems pretty likely to happen in such a long time period. For the sake of simplicity, then, it was decided to adopt a thermal load copying exactly the values of power extracted by the HT, in order to avoid possible excessive mismatches. This solution allows for the exploitation of the same input signal for the two pumps and consequently minimizes fluid level fluctuations, zeroing the possibilities of tank depletion or overload.

Integration configuration

The level of fluid stored inside the two tanks went under small fluctuations, never being close to the upper or lower limits. In particular, CT fluid level resulted to be substantially constant over the year, with a minimum height of 3.96 m and a maximum of 4.00 m, while the HS experienced slightly higher fluctuations between 3.94 and 4.29 m.

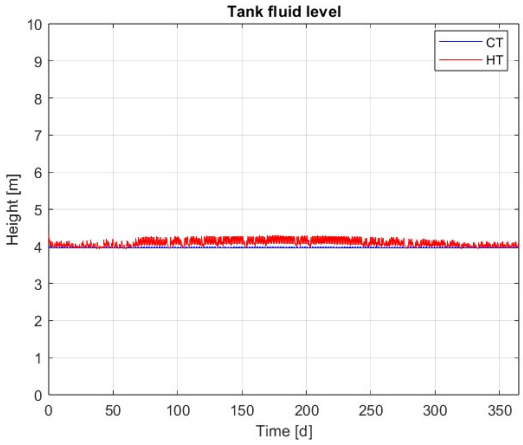

Figure 3.45: Yearly tank's medium levels - Integration

Temperatures, on the other hand, are characterized by more important variations, but resulted to always be under control, as visible in Figure 3.46. More specifically, the cold storage fluid registered an initial peak of 563 K, which stabilizes after three days to a constant value of 533 K, maintained for the rest of the year, while the hot storage experienced temperatures between

572 and 818 K, and is characterized by a macro-trend that replicates the variation of DNI average values during the different seasons. The upper limit temperature of 833 K was not exceeded, instead. In the first days, even the HT features an important drop which, in any case, does not lead the system to significant deviations from its expected behavior. These abnormal values have been related to computational reasons that will be consolidated in future studies due to their potential complexity. A possible issue, rather, is represented by the minimum temperature reached by the medium stored inside the CT, which in this case was 10 K below the safety threshold of 543 K. It has to be considered, however, that the *Integration* mode was not designed to guarantee this condition with particularly adverse environmental conditions. Results, all in all, can be considered satisfactory.

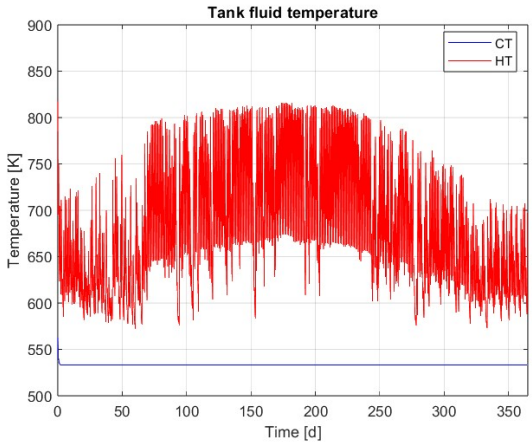

Figure 3.46: Yearly tank's medium temperatures - Integration

For what concerns the fluid inside the receiver tube (see Figure 3.47), it is clear how the mass flow rate regulation system is able to effectively keep its minimum and maximum temperature between two constant levels almost all over the year. While the lowest detected temperature is 511 K, lower than the minimum CT temperature due to the losses affecting molten salts while flowing through the receiver, the maximum value registered results to be 826 K, not that far from the target 818 K, but still lower than the limit of 833 K. The average fluid temperature throughout the year results 573 K. These values confirm how the *Integration* configuration can't be exploited throughout the whole year, but must be wisely adopted at the occurrence of sufficiently favorable weather conditions.

Figure 3.48 highlights how P2, the pump dedicated to the extraction of fluid from the HT, works on a wide range of values, from a minimum of 20.8 kg/s, which was found to be the minimum flow necessary to guarantee

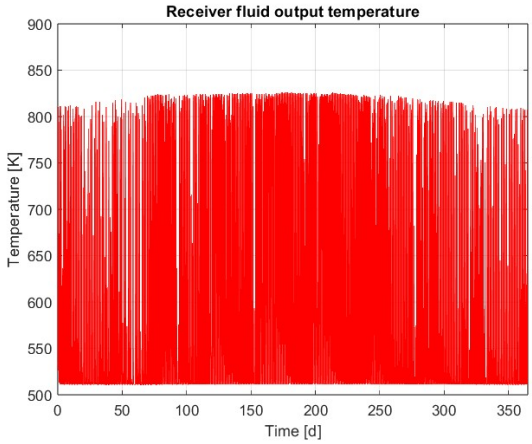

Figure 3.47: Yearly receiver outlet temperature - Integration

molten salts a safety temperature [3], and a maximum around 103.9 kg/s, implemented in the hottest days of the year, when the amount of energy stored inside the thermal vector is high and needs to be dissipated quickly in order to avoid overheating.

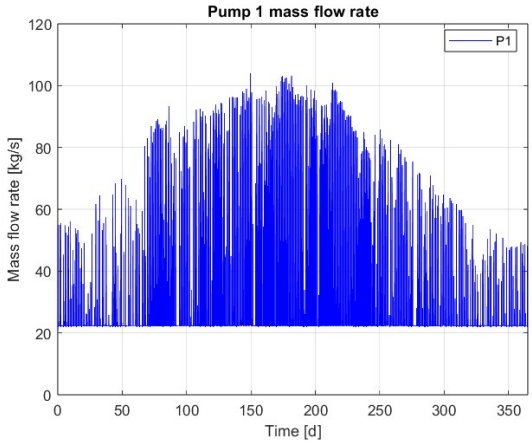

Figure 3.48: Yearly SB pump mass flow rate - Integration

In particular, the LFR branch minimum mass flow rate is 18.0 kg/s, as defined in the *MFR_controller* block, while the GFH branch is distinguished by values varying between 2.8 and 4.4 kg/s, as described in Figure 3.49.

An important element to consider is the non-perfect overlapping of mass

[3]In *Integration* mode, this condition has demonstrated not to work all year long, so an higher minimum mass flow rate is probably needed. Adjustments were not performed since, as already mentioned, this configuration was not devised to be exploited overnight or in particularly hostile environmental conditions.

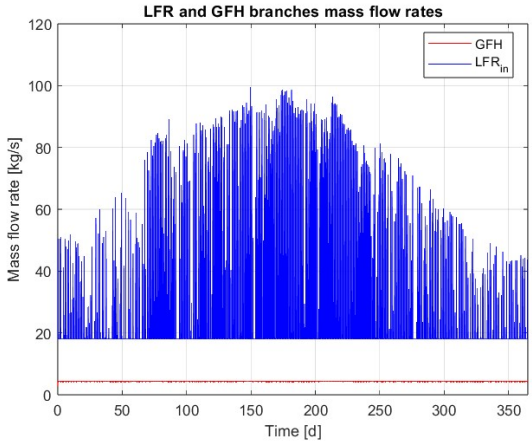

Figure 3.49: Yearly SB and GFH mass flow rate - Integration

flow rate values between the LFR inlet and outlet, with a deviation assessed in the interval $[-1.5/+1.0]$ kg/s, as visible from Figure 3.50. In order to avoid discrepancies between the mass withdrawn from the HT and the one ejected at the receiver's end, which would cause medium level to fluctuate, P2 mass flow rate has been slightly deviated from P1's, using as input signal the sum of the two values detected at the receiver and GFH outlets. P1 and P2 mass flow rates, though, result substantially coincident for most of the time.

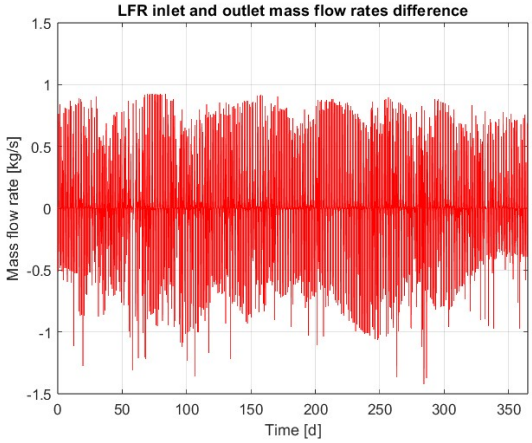

Figure 3.50: Yearly receiver input and output mass flow rate difference - Integration

The annual thermal energy yield results to be 72.8 GWh, 57.0 of which (78.3%) were obtained from the solar field, while 15.8 (21.7%) from the gas-fired heater. The SB share results, in relative terms, 8.5% lower than the

corresponding renewable fraction obtained with the daily simulation seen in Subsection 3.4.1, which is a totally coherent value, though, since the model was simulated in a summer day, when the availability of solar power is considerably greater. The plant's power generation is described in Figure 3.51, while thermal losses build up to a total of 15.4 GWh, around 17.5% of the total amount of energy reaching the receiver. As previously mentioned, in order to maintain fluid levels inside the two tanks under control, the PB load trend was set equal to the SB power production.

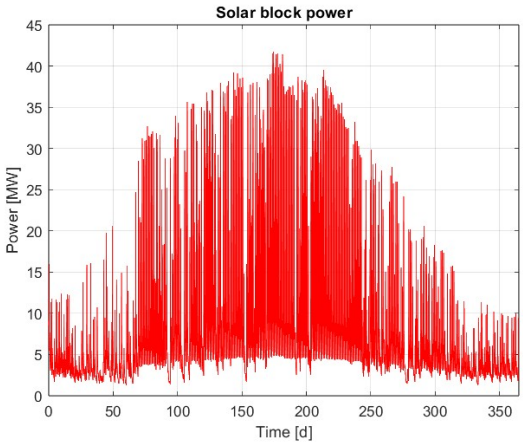

Figure 3.51: Yearly power generation - Integration

Performances can be considered more than satisfying: the whole simplified model, made up of a system of 474 equations, took only 235 s to run. Given these results, a decrease in time step length could be evaluated in order to increase the accuracy of simulations.

Antifreeze configuration

Similarly to the previous configuration, Figure *Antifreeze* ensures very low medium fluctuations inside the two tanks. The cold fluid level varies between 4.00 and 4.06 m, while the hot one evolves between 3.93 and 4.29 m.

Thanks to the mass flow rate regulation system, HT temperatures result pretty much the same as the previous configuration, with the exception of the maximum temperature reached, now 567 K (earlier it was 572 K), but the biggest differences are related to the CT. It must be noted how this parameter is subject to important fluctuations in time, while *Integration* mode saw, with the exception of a short initial period, a constant temperature throughout the whole year. This anomalous behavior, after an inspection of the *PartialStorage* script, resulted to be originated by the same numerical reason encountered earlier, which causes the enthalpy value to diverge between the PB outlet and the CT inlet, causing fluctuations in

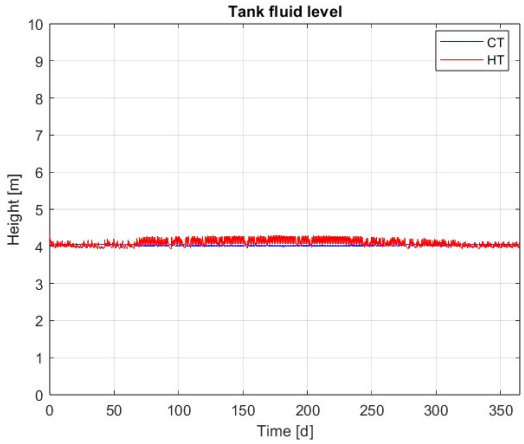

Figure 3.52: Yearly tank's medium levels - Antifreeze

temperature levels. Luckily, this computational issue does not lead to major consequences, so its resolution can be postponed to further analysis. This time, on the other hand, temperatures do not drop below 547 K, a few degrees over the safety level necessary to avoid freezing, while the maximum stands at 600 K. This information proves how the *Antifreeze* configuration is able to manage harsher weather conditions compared to the alternative studied before.

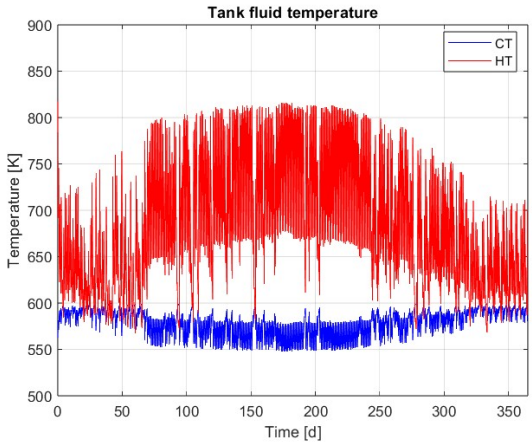

Figure 3.53: Yearly tank's medium temperatures - Antifreeze

Similarly to what has been seen for the two tanks, the receiver's fluid does not show any particular difference for what concerns top temperatures, whose peak is located at 824 K, only 2 K less than the *Integration* configuration. Minimum values, on the contrary, result sensibly greater than the ones seen before, with the lowest value now corresponding to 534 K,

23 K more than before. The reason behind this can be found in the heavier GFH exploitation (see Figure 3.56), which is able to provide a higher baseline power, but the computational issues discussed in the previous lines make this assumption not necessarily reliable. The average fluid temperature throughout the year, now equal to 608 K, results significantly hotter than the one found in *Integration* mode (+35 K).

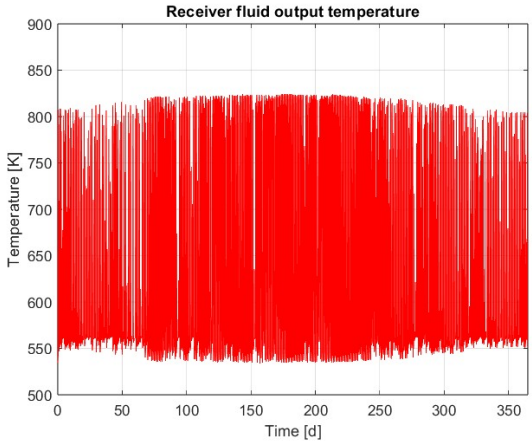

Figure 3.54: Yearly receiver outlet temperature - Antifreeze

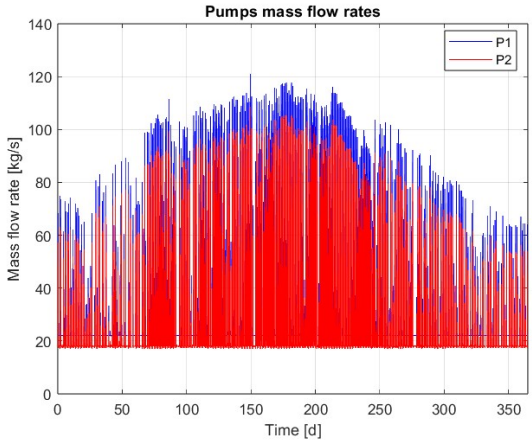

Figure 3.55: Yearly pumps mass flow rate - Antifreeze

The *Antifreeze* mode, in fact, causes pumps to operate at higher mass flow rates, this time between 21.9 and 120.8 kg/s. In particular, the greatest difference concerns the GFH branch, which now works between 3.9 and 12.3 kg/s (maximum mass flow rate increased 2.8 times compared to the other configuration), but even the solar branch increased its peak mass flow by 9.0 units.

Even in this case, the receiver tube is affected by discrepancies in the mass flow rates detected at the inlet and outlet sections, which resulted substantially coincident to the ones encountered in Figure 3.50.

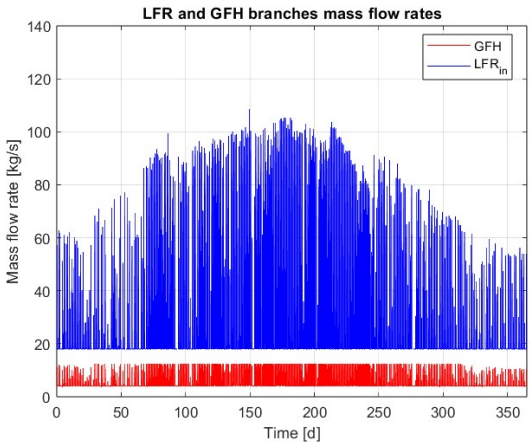

Figure 3.56: Yearly SB and GFH mass flow rate - Antifreeze

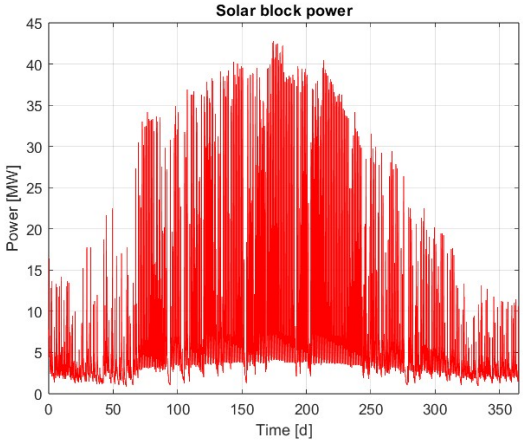

Figure 3.57: Yearly power generation - Antifreeze

This time, the annual thermal energy yield resulted to be 70.1 GWh, slightly lower than the amount produced in the alternative configuration. More specifically, 54.3 GWh (77.5%) are obtained from the solar field, while 15.8 GWh (22.5%) from the gas-fired heater. The reduced amount of energy generated from the plant (-3.7%) must all be attributed to the renewable side, which is in this case characterized by a lower yield. The reason behind that lies in the greater temperatures affecting molten salts inside the receiver, which cause thermal losses to build up to a total of 18.1 GWh per

year, in spite of the same climatic conditions to which the system is subject. The power generated from the solar field is provided in Figure 3.57.

The simulation proved to be satisfactorily efficient even computation-wise. The 471 equations needed to model the CSP plant, indeed, took only 322 s to run, 87 s more than the *Integration* configuration, probably due to the higher computational demand required in this case by the PID-based flow controller.

3.4.3 Hybridization

In order to explore potential advantages in the hybridization of the Partanna CSP plant, a PV field with an area of 27 735 m^2, equal to a third of the CSP mirror field, was combined with it.

A *PhotovoltaicModule* block was created in order to compute, given an input consisting of DNI, wind speed, and ambient temperature, the electric power generated by the photovoltaic field. In order to provide a more realistic definition of PV power values, it has been decided to adopt clear sky conditions, rather than STC (Standard Testing Conditions), using NMOT (Normal Module Operating Temperature) to describe more accurately solar cell temperatures. In particular, the most relevant equations used to model PV operation are provided below [18].

$$T_c = T_{amb} + (NMOT - T_{amb,ref}) \cdot \frac{G}{G_{NMOT}} - C \cdot W_{spd} \tag{3.5}$$

Equation 3.5 defines PV cell temperature as a function of the ambient temperature T_{amb}, solar irradiance G, corresponding to DNI, and wind speed W_{spd}. Additional parameters like NMOT, reference ambient temperature $T_{amb,ref}$, NMOT reference irradiance G_{NMOT}, and wind coefficient C are all defined in Table A.6. This last parameter, in particular, allows the system to take into account variable wind speeds in the definition of the module's temperature: the stronger the wind, the more intense the convection mechanisms, the colder the PV module.

$$\eta_{irr} = 1 - \frac{G_{lim}}{G} \tag{3.6}$$

Equation 3.6, instead, models how PV power generation efficiency varies with irradiance. G_{lim} constitutes the limit below which there can be no power production, assessed at 20 W/m^2, and when irradiance levels overcome this value, η_{irr} is set to 0.

$$P_{max,STC} = \eta_{STC} \cdot G_{STC} \cdot S_{PV} \tag{3.7}$$

Equation 3.7 defines the photovoltaic field maximum power in STC, which depends on the total area S_{PV} covered by the site, the module's reference efficiency η_{STC}, and the STC reference irradiance G_{STC}. This is considered the maximum amount of electric power the site can possibly produce in ideal conditions.

$$P_{gen} = P_{max,STC} \cdot \frac{G}{G_{stc}} \cdot (1 + \gamma_{P_{max}} \cdot (T_c - T_{STC})) \cdot \eta_{irr} \tag{3.8}$$

Equation 3.8, instead, describes the actual site photovoltaic power production as a function of irradiance and cell temperatures. In addition to the previously discussed parameters, this variable depends on an additional element, called "power thermal coefficient" ($\gamma_{P_{max}}$), describing how cell temperature affects PV power generation. The hotter the module, in fact, the worse its performance.

Now that power generation mechanisms have been cleared up, the way the PV system interacts with the CSP plant has to be defined. The component that, in particular, needed to be adjusted in order to make hybridization possible is *StorageHeat* (see page 20), dedicated to the resolution of energy balances in order to define molten salts temperature.

The PV power distribution system is based on energy levels. Here is the control sequence performed:

1. Given the HT fluid height, the maximum energy content that can possibly be stored by molten salts without exceeding a limit temperature of 818 K is computed.

2. Once this value gets determined, the actual energy stored inside the fluid is calculated and compared with this limit value.

3. If it results lower, it means that the temperature is below 818 K, so an additional power injection is possible, while, on the contrary, if it is greater, it implies that we are over the limit and no additional power is required.

4. Once the HT medium condition is known, an analysis has to be carried out on potentially available photovoltaic energy. In the case the HT fluid results below its temperature limit, PV availability and energy gap are compared.

- If the energy gap is greater than the availability from PV, all its power is directed towards the HT and turned by means of a resistance into thermal energy in order to increase medium's energy level.
- In the case the availability is greater than the gap, only the fraction necessary to get the fluid to the energy limit is converted into thermal energy, while the remaining share is directly injected into the grid.

In the case the fluid has a temperature above the limit, all the power from the PV is directed towards the electrical grid.

5. This set of controls is iterated at every timestep.

A very important aspect to stress is the reason why the PV power management system has been developed in this way. Normally, indeed, the priority is to inject into the grid as much photovoltaic electric power as possible, due to its lower cost and the greater efficiency of the process, while CSP generation is exploited to meet the additional power demand when PV is not able to cover it all by itself. On the opposite, in the case the photovoltaic field is able to overcome the electric demand, then the supplementary share is discharged into the tanks in order to preserve at least a portion of it, avoiding curtailing. By turning it directly into thermal power, though, roughly 60% of it gets lost into the thermal-to-electric conversion process operated by a standard Rankine cycle, while a direct grid injection efficiency is only determined by the DC-to-AC conversion process, operated by inverters, whose losses are often lower than 5% when PV power is close to the inverter's rated value [20]. In addition, exploiting photovoltaic energy as previously described determines a further increase in the HT temperature, which possibly constitutes an additional risk for salts overheating and consequent degradation.

Given the simplified configuration considered for the simulations, however, which involves no possible mismatch between power availability and demand, this represents the only way to introduce a "smart" interaction between the storage and PV systems, as well as a test to determine the actual capabilities and potential limits of the model. Otherwise, all the electricity produced by the PV field would have been directly injected into the grid, causing the two systems not to be hybridized, but simply work in parallel as two distinct renewable power generation systems. The decision not to inject additional thermal power into the CT, instead, was due to the irrelevant impact this solution had on system performances. The greater the temperature with which molten salts were pumped out of the cold storage, the higher the regulation system set P1 mass flow rate, which determined no substantial increase in salt temperature at the outlet of the receiver.

Simulations have been performed for both simplified model configurations.

Figure 3.58 describes the photovoltaic power production over time, which is common to both *Integration* and *Antifreeze* configurations. This source appears to ensure a pretty much constant power generation throughout the year, characterized by daily peaks most of the time comprised between 4 and 5 MW and overnight values of 0 W due to the absence of solar radiation. The annual energy yield of such a photovoltaic system was assessed to be 24.0 GWh.

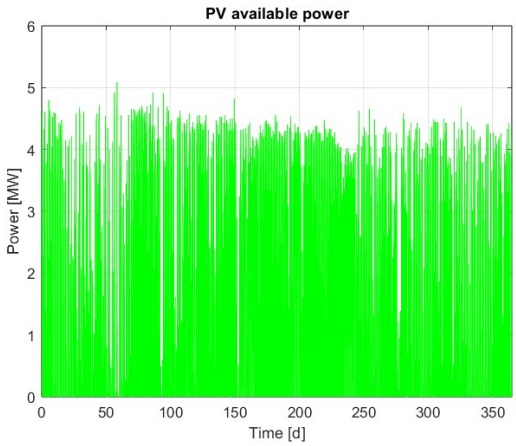

Figure 3.58: Yearly PV power generation

Integration configuration

CT fluid level resulted to be substantially constant over the year, with a minimum height of 3.96 m and a maximum of 4.00 m, while the HS experienced slightly higher fluctuations between 3.94 and 4.30 m. These values result almost coincident with the ones seen in the configuration excluding PV, even if, in the cold season, slightly greater level fluctuations inside the HT have been detected, probably attributable to temperature differences.

Temperature-wise, the cold storage fluid registered the exact same values as before, while the hot storage experienced marginally higher temperature extremes, now between 574 and 822 K (+2 and +4 K compared to the CSP-only system). Referring to the macro-trend, HT values result considerably higher than before, especially in the coldest months, due to a significant injection of energy from the PV side.

For what concerns the fluid inside the receiver, with a minimum temperature of 511 K and a maximum of 826 K, values result to be coincident with the solar-only plant, and this is due to the configuration of the system, which exploits PV energy to exclusively heat up the HT, while the CT is not

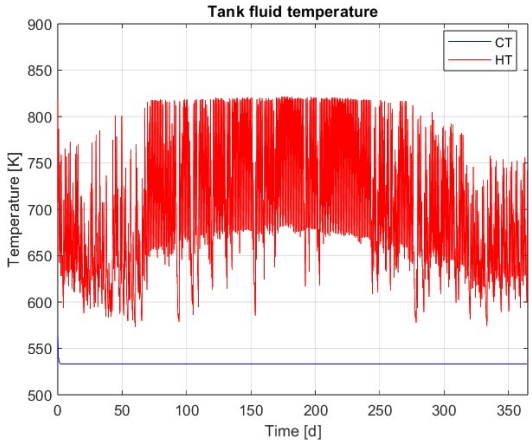

Figure 3.59: Yearly tank's medium temperature - Hybridized Integration

affected since the surplus energy share is completely absorbed by the heat exchanger simulating the load. The average fluid temperature throughout the year is 573 K, identical to the one found in the CSP-only configuration.

Figure 3.60, in particular, describes the average daily temperature difference inside CT, HT, and LFR throughout a typical year.

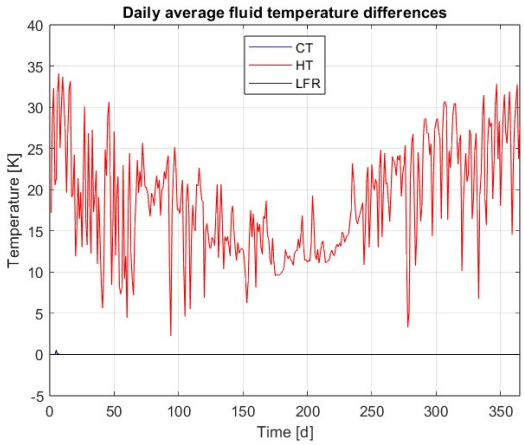

Figure 3.60: Daily average temperature differences between standard and hybridized models - Integration

For what concerns mass flow rates, P1 sees its minimum value increasing from 20.8 to 22.1 kg/s, while the peak is still at 103.9 kg/s. More specifically, the lowest rate at which salts flow through the LFR branch is 18.0 kg/s, as previously defined, while the GFH branch mass flow varies between 4.1 and 4.4 kg/s, higher than the solar-only configuration, where the smaller value detected was 1.3 kg/s less. Considering that the mismatch between mass

flow rate values at the receiver's inlet and outlet did not change, P1 and P2, in spite of the limited differences that emerged, result substantially coincident.

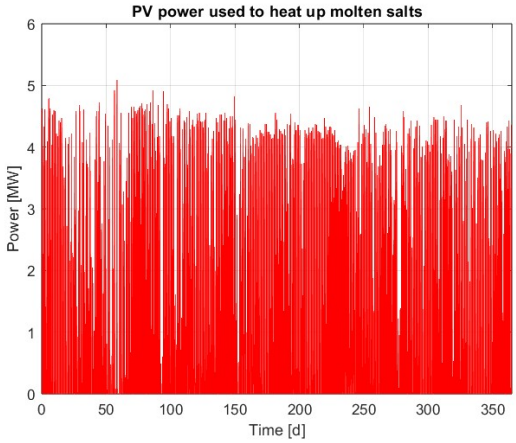

Figure 3.61: Yearly electric-to-thermal power conversion - Hybridized Integration

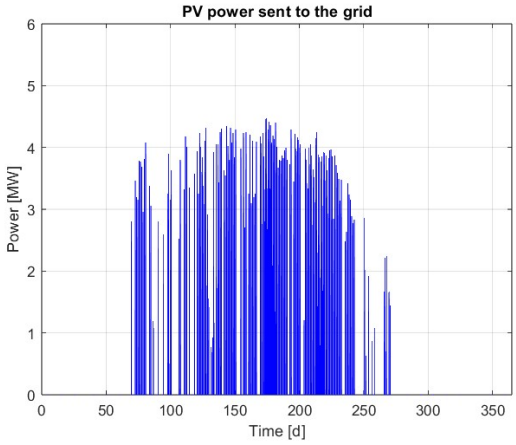

Figure 3.62: Yearly grid-injected electrical power - Hybridized Integration

Considering the photovoltaic component, the way the produced electrical power is managed depends on environmental and weather conditions. Figures 3.61 and 3.62, more precisely, provide a clear representation of both the megawatts turned into heat to provide additional support to the HT and the electricity directly injected into the transmission system. Since the cold season is characterized by an insufficiently high solar energy provision, the amount of power directed to the grid is substantially null, and this is because most of it gets converted into heat in order to increase the temperature of

HT molten salts. In the hot season, on the contrary, due to more favorable environmental conditions and stronger irradiation, a significant share of the energy generated by the PV field (up to 50.7% of the total yield) is directly injected into the grid. A dedicated description of this regulation process is provided by Figure 3.63.

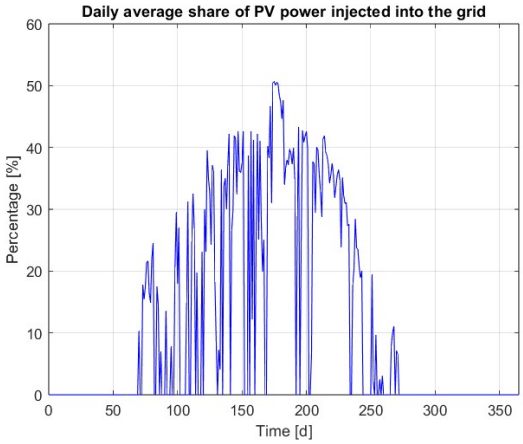

Figure 3.63: Daily average grid injection power share - Hybridized Integration

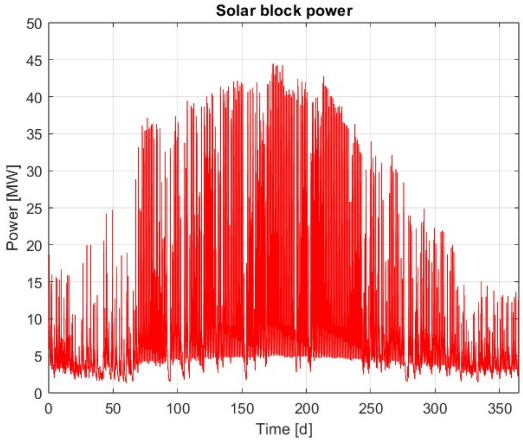

Figure 3.64: Yearly power generation - Hybridized Integration

The annual thermal energy yield results to be 81.7 GWh, 12.2% more than the standard configuration. More specifically, 57.0 GWh (69.8%) have been obtained from the LFR, 15.8 (19.3%) from the GFH, and 8.9 (10.9%) derive from the photovoltaic energy injected into the HT. Thermal losses build up to a total of 15.4 GWh per year, which is the same value characterizing the original model since the additional share provided to the heat

storage, due to its adiabatic walls, is not subject to any dissipation. The hybridized system also needs to consider an additional share of 1.9 GWh produced by the PV modules and directly injected into the grid with no need for thermal conversion. Figure 3.64 shows the annual trend of the CSP-related power generation, which takes into account both the standard CSP power generation and the additional support provided by PV thermal energy.

In spite of the additional complexity constituted by hybridization, corresponding in practical terms to 10 more equations, computation time resulted only marginally altered (261 s).

Antifreeze configuration

In *Antifreeze* mode, the cold fluid height varies between 4.00 and 4.06 m, while the hot one oscillates between 3.93 and 4.30 m, substantially the same values observed in the solar-only configuration.

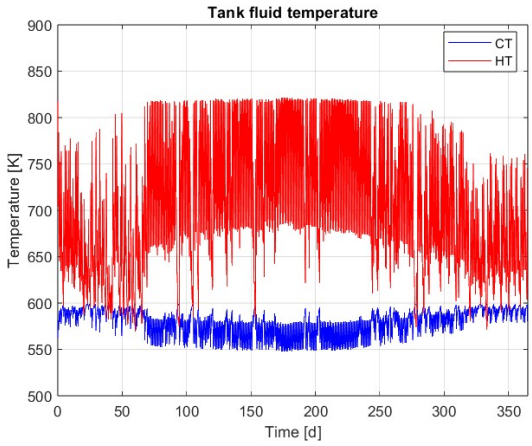

Figure 3.65: Yearly tank's medium temperature - Hybridized Antifreeze

HT temperature extremes result pretty much the same as the previous configuration, with values between 569 and 822 K, but the average temperature increased significantly in the cold season. CT temperatures are approximately equivalent to the original counterpart, with values between a minimum of 548 K and a maximum of 600 K.

The receiver's fluid temperatures, once again, did not change from the standard configuration values. The average fluid temperature throughout the year, indeed, is still 608 K, 35 K hotter than the one detected in *Integration* mode. Figure 3.66, in particular, describes the average daily temperature difference inside CT, HT, and LFR throughout a typical year.

The activity registered for the pumps, instead, results to be coincident with the CSP-only plant version.

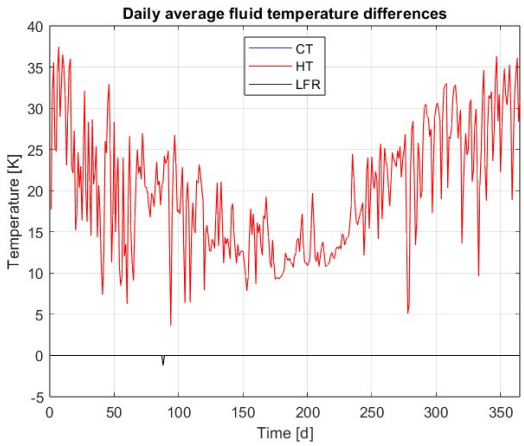

Figure 3.66: Daily average temperature differences between standard and hybridized models - Antifreeze

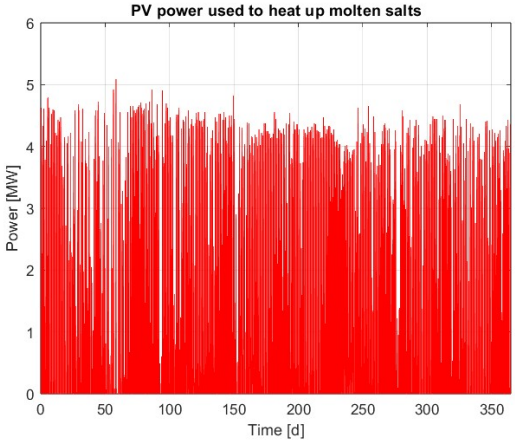

Figure 3.67: Yearly electric-to-thermal power conversion - Hybridized Antifreeze

For what concerns the photovoltaic section, the *Antifreeze* configuration is characterized by a lower PV power conversion rate, especially in the colder months, when the GFH activity is able to compensate for part of the energetic deficit inside the HT, decreasing the integration demand requested from the photovoltaic system. As a consequence, while the peak sharing value increases to 51.4% (+0.7%), around 0.1 GWh of additional electrical energy is directly dispatched to the grid.

The yearly thermal energy yield resulted to be 78.9 GWh, 12.6% greater than the solar-only plant configuration, but still slightly lower than the amount produced in the hybridized *Integration*. More specifically, 54.3 GWh

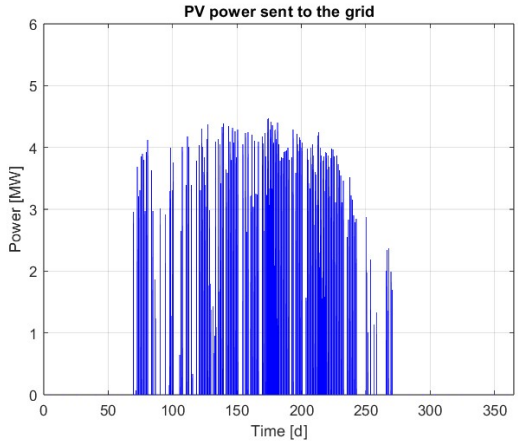

Figure 3.68: Yearly grid-injected electrical power - Hybridized Antifreeze

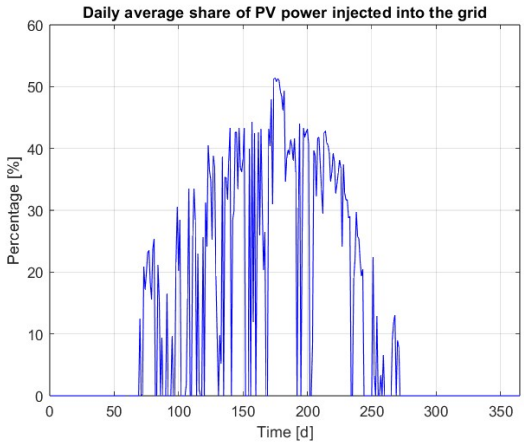

Figure 3.69: Daily average grid injection power share - Hybridized Antifreeze

(68.8%) have been obtained from the solar field, 15.8 (20.0%) from the gas-fired heater, and 8.8 from photovoltaic conversion (11.2%). The limited reduction in LFR activity is only determined by the greater losses characterizing the system, which in this configuration, due to a greater average receiver tube medium temperature, build up to a total of 18.1 GWh per year. An additional share of 2.0 GWh, produced by the PV modules, but not converted into thermal energy, is dispatched to the transmission system. The plant's power generation trend is reported in Figure 3.70.

Computation time reported only a slight increase of 7 s compared to the standard power plant configuration, growing from 322 to 329 s.

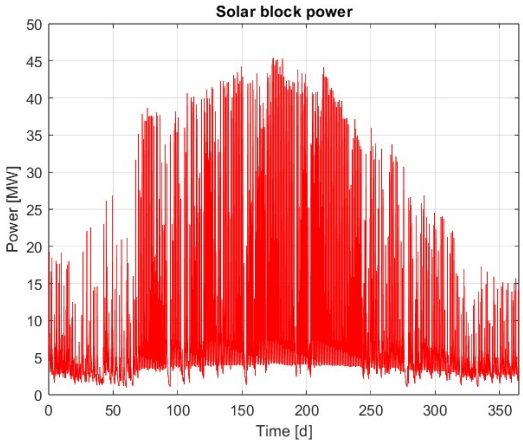

Figure 3.70: Yearly power generation - Hybridized Antifreeze

3.5 Techno-economic analysis

To properly evaluate the possible benefits of hybridization, thermal results have been exploited to compare the different configurations examined from an economical point of view. Starting out from the data reported in Table F.1, both fixed and variable costs of the plants have been calculated in order to define their characteristic Levelized Cost Of Energy (LCOE), which "can be thought of as the average total cost of building and operating the asset per unit of total electricity generated over an assumed lifetime" [14]. It is a fundamental parameter in the long-term comparison of different energy-producing technologies, which allows comparing them regardless of a different lifespan, capital cost, annual electricity output, and risk levels. The LCOE [17] is defined by the following equation:

$$LCOE = \frac{CAPEX \cdot \frac{d \cdot (1+d)^n}{(1+d)^n - 1} + OPEX}{NAEO}, \tag{3.9}$$

where $CAPEX$ is the capital expenditure of the plant, including contingencies, EPC, and owner costs, d is the discount rate, $OPEX$ the annual cost for operations and maintenance, n the lifetime of the plant, and $NAEO$ its net annual electrical energy yield in MWh.

Calculations, which were performed by combining structural and technical data from Appendix A, in addition to the energetic results from Section 3.4, produced the LCOE values reported in Table 3.5.

A comparison between the *Integration* and *Antifreeze* configurations, as expected, finds the first slightly cheaper than the alternative. Since the

capital cost of the two plants, computed around 50.5 M EUR when contingencies, EPC, and owner's costs are considered, is exactly the same, the only difference is constituted by the annual energy yield, respectively 29.1 and 28.0 GWh. This element makes the energy produced by the plant in *Antifreeze* mode a little bit more expensive (+8.43 EUR/MWh). The trend holds true even for the hybridized counterparts.

Configuration	Integration	Antifreeze
CSP plant	218.86	227.29
CSP + PV hybrid plant	258.84	266.71

Table 3.5: LCOE in EUR/MWh$_{el}$

Moving on to the analysis of the benefits brought about by hybridization, results highlight a sensibly negative impact on LCOE values, which experience increments of 18.3% for the *Integration* configuration (+39.98 EUR/MWh), and 17.3% in *Antifreeze* conditions (+39.42 EUR/MWh). The additional energy yield provided by the PV system, indeed, respectively of 5.5 and 5.6 GWh, results insufficient to compensate for the additional capital expenditure required to complement the CSP plant with a photovoltaic solar field, assessed around 20.5 M EUR. On the other hand, though, as mentioned on page 70, the photovoltaic power management system is not optimized to minimize the LCOE, but rather to increase CSP performances, trying to introduce a dynamic interaction between the two hybridized subsystems with the final purpose of testing the actual capabilities of the Open Modelica model. A cost-oriented management of the 24.0 GWh produced annually by the PV plant would have probably generated a substantial drop in LCOE values.

Chapter 4

Future developments

In perspective, the present work could constitute the starting point of further investigations. The final CSP plant model, indeed, has proved capable of running yearly simulations requiring relatively low computation times, in addition to supporting the additional complexity constituted by possible hybridized configurations, but many areas could still be objects of improvement.

In the current condition, the most limiting aspect is clearly represented by the inability to manage decoupled power generation and load. The absence of suitable control systems, able to dynamically regulate the levels of molten salt inside the two thermal storage units, constitutes a huge constraint to the exploitation of such virtual models into possible real-world applications and studies.

For what concerns hybridized models, instead, the previously mentioned capability to handle mismatched power production and demand could enable the possibility to refine how CSP and PV systems interact with each other, privileging the optimization of LCOE. This could be obtained by prioritizing the dispatch of PV-generated electric power, exploiting the possibility of storing it as thermal energy only when the generation overcomes the load. This solution could extend the capability of the CSP side to cover the energetic demand when solar irradiance is low or not available at all, increasing the overall capacity factor characterizing the plant.

Another improvable aspect is constituted by the in-depth study and resolution of the numerical issues emerged in annual simulations for what concerns the behavior of molten salts inside the cold storage. What has been detected, in particular, is a mismatch between the values of enthalpy characterizing the medium between the PB outlet and the CT inlet, which generates manageable, but still relevant, fluctuations in molten salt temperatures.

Chapter 5

Conclusions

This experimental thesis presents the work accomplished in the research and comparison of alternative solutions oriented to reducing the numerical complexity of an existent CSP system virtual model, with the ultimate goal of defining the best balance between the accuracy of results and the computational cost, enabling simulations over a year-long time range.

The original version was created exploiting Modelica, a unified object-oriented language for physical systems modeling, and consisted of a model able to accurately predict, over short transients, the optical and thermal-fluid-dynamic performance of CSP systems based on the parabolic trough or the linear Fresnel reflector scheme. This study, in particular, considers the Partanna solar plant, which makes use of the LFR technology and a mixture of molten salts as heat transfer fluid.

The attention has been concentrated on the two components requiring the highest number of equations to be modeled, and thus constituting the elements requiring the greatest computational effort to be simulated, namely the heat storage system and the receiver, which have been simplified under several different aspects.

The thermal storage was initially deprived by the sub-model dedicated to the simulation of the air volume enclosed between the molten salts free-surface and the tank's lid, necessary in order to define part of the convective heat losses affecting molten salts. The next step has been the substitution of the storage top, side, and bottom multi-layered surfaces with adiabatic walls, neglecting in this way the radiative and convective heat transfer mechanisms modeling the energy fluxes exchanged between the medium and the external environment. The combined adoption of these two solutions were proved to just minimally affect results accuracy, causing, on the opposite, a significant reduction in the number of equations needed to model the component, which led to substantial improvement for what concerns run times.

The receiver, instead, has been tackled differently, not acting on the elimination of negligible thermal mechanisms, but rather on reducing its

degrees of discretization. On the azimuthal dimension, in order to grant higher accuracy, this component was originally divided into an upper and a lower half since these two elements are subject to very different irradiance levels and, therefore, are characterized by particularly dissimilar values for what concerns major indicators like temperature and heat losses. On the axial dimension, on the other hand, the component is split into multiple sub-volumes, each one analyzed independently but able to communicate with the adjacent ones. This solution is adopted in order to describe the evolution of properties like temperature and losses as the axial coordinate changes. Reducing the number of these volumes to just one means losing the possibility to trace molten salts behavior along the axis, but leads to sensible performance improvements, maintaining at the same time a good level of accuracy.

The evolution of daily run times before and after optimizing the *Integration* and *Antifreeze* model configurations, along with the annual results, is provided in the tables below:

Property	Integration	Antifreeze
Number of equations	2771	2776
Computation time [s]	23.77	29.01

Table 5.1: Original model daily simulation performance

Property	Integration	Antifreeze
Number of equations	443	448
Computation time [s]	1.85	1.96

Table 5.2: Simplified model daily simulation performance

Property	Integration	Antifreeze
Number of equations	474	471
Computation time [s]	235	322

Table 5.3: Simplified model annual simulation performance - Standard configuration

The possibility to simulate the Partanna CSP plant over a typical year in reasonable times allowed to obtain precious results reflecting the general

performance of such a system. These data was then exploited in the definition of a techno-economic analysis, useful for the evaluation of potential investments or the prediction of potential ranges for the cost of produced energy.

Additionally, the two models were tested in an hybridized configuration, where the CSP system has been combined with a photovoltaic field and communicated with it through a specific control logic based on the relationship between the CSP hot tank medium energy level and PV power generation. This control system, though, is not oriented to the minimization of LCOE, and does not reflect the real control mechanisms employed in the industry, but rather wants to assess the model capabilities of supporting possible integrations with alternative renewable power systems, which proved to be well supported. The computational performances obtained for the hybrid layout are reported below:

Property	Integration	Antifreeze
Number of equations	484	481
Computation time [s]	261	329

Table 5.4: Simplified model annual simulation performance - Hybridized configuration

In perspective, it would be extremely interesting to further refine the optimized model in order to enable, through a suitable CT and HT level control system, a correct functioning under decoupled power generation and load, as well as to adjust the way the CSP and PV systems interact with each other in the hybridized configuration for the purpose of obtaining optimized LCOE values.

Appendix A

Partanna solar station data

This appendix summarizes the available data for the Partanna CSP plant.

Property	Value
Solar field azimuth (South = 0°, West > 0°) [°]	-26.19
Collector tilt angle [°]	0
Number of solar loops	9
Length of the solar field [m]	768.4
Mirror width [m]	0.752
Number of parallel mirrors	16
Distance between adjacent mirrors [m]	1
Focal length [m]	7.4
Length of the receiver tube [m]	817.6
Outer/Inner absorber tube diameter [m]	0.070 / 0.064
Outer/Inner glass envelope diameter [m]	0.125 / 0.119
Reference optical efficiency (zenith)	0.704
Surface cleanliness efficiency	1
Shadow efficiency	1
End-line efficiency	1

Table A.1: Solar station and receiver data

Property	Value (CT)	Value (HT)
Inner diameter [m]	13	13
Height [m]	10	10
Maximum fluid level [m]	7.34	7.92
Minimum fluid level [m]	0.66	0.66
Initial fluid level [m]	4.00	4.29
Wall thickness [m]	0.003	0.003
Insulation thickness [m]	0.200	0.300
Basement thickness [m]	1.50	1.50
Medium emissivity	0.95	0.95
Tank surface emissivity	0.50	0.50

Table A.2: Cold tank (CT) and hot tank (HT) heat storage data

Property	Value (I)	Value (A)
Thermal power [kW]	1800	1800
Initial mass flow rate [kg/s]	4	12
Initial inlet temperature [K]	563	563
Initial outlet temperature [K]	818	653
Pressure loss coefficient [1/kg/m]	0	0

Table A.3: *Integration* (I) and *Antifreeze* (A) mode gas-fired heater data

Property	Value (I)	Value (A)
Flow coefficient [m^2]	$5 \cdot 10^{-4}$	$5 \cdot 10^{-4}$
Type of controller	P P controller	P P controller
Gain	0.1	0.1
Initial mass flow rate [kg/s]	4	12
Initial opening value	0.65	1
Initial mass flow rate set point [kg/s]	4.4	12.3
Initial value of output	0.65	1
Mass flow rate set point [kg/s]	4.4	12.3

Table A.4: *Integration* (I) and *Antifreeze* (A) mode flow controller data

Property	Value
Initial mass flow rate [kg/s]	18
Initial inlet temperature [K]	818
Initial outlet temperature [K]	563
Pressure loss coefficient [1/kg/m]	$8 \cdot 10^5$
Rankine cycle efficiency	0.40

Table A.5: Power block data

Property	Value
Available surface [m^2]	27 735
STC module efficiency	0.21
Power thermal coefficient [1/K]	-0.0045
NMOT [K]	318
Wind-related temperature reduction coefficient [K/(m/s)]	1
Reference ambient temperature [K]	298
NMOT reference irradiance [W/m^2]	800
Inverter efficiency	0.98

Table A.6: Photovoltaic field data

Appendix B

Materials properties

This appendix provides the thermal and physical properties of the materials implemented in the Partanna CSP lumped-parameter model.

Molten salts: mixture of 60% $NaNO_3$ (sodium nitrate) and 40% KNO_3 (potassium nitrate), used as heat transfer fluid by the CSP system and operated between a minimum temperature of 533 K, which constitutes their freezing point, and a maximum of 833 K, over which they degrade.

Property	Value (T expressed in °C)
Density [kg/m^3]	$2090 - 0.636 \cdot T$
Dynamic viscosity [mPa · s]	$22.714 - 0.12 \cdot T + 2.281 \cdot 10^{-4}$ $\cdot T^2 - 1.474 \cdot 10^{-7} \cdot T^3$
Specific heat capacity [J/(kg · K)]	$1443 + 0.172 \cdot T$
Thermal conductivity [W/(m · K)]	$0.443 + 1.9 \cdot 10^{-4} \cdot T$
Minimum operational temperature [K]	533
Maximum operational temperature [K]	843

Table B.1: Molten salts properties

CERMET: spectrally-selective coating material constituting one of the absorber tube layers, able to guarantee high absorptivity of the external radiation in order to heat up the transfer fluid.

Property	Value (T expressed in °C)
Absorptivity	0.95
Emissivity	$2.2 \cdot 10^{-7} \cdot T^2 + 0.07513$

Table B.2: CERMET properties

AISI 321: metallic material selected for the absorber tube inner layer in order to exploit the infrared radiation re-emitted from the transfer fluid to get what is called "infrared reflection".

Property	Value (T expressed in K)
Density [kg/m^3]	8090
Thermal conductivity [W/(m $\cdot$ K)]	$0.0150 \cdot T + 10.4$
Specific heat capacity [J/(kg $\cdot$ K)]	500

Table B.3: AISI 321 properties

Borosilicate glass: material making up the receiver's outer glass coating, featuring high levels of transmittance for solar radiation, and low values for the receiver's thermal re-emitted radiation.

Property	Value
Density [kg/m^3]	2230
Thermal conductivity [W/(m $\cdot$ K)]	1.1
Specific heat capacity [J/(kg $\cdot$ K)]	850

Table B.4: Borosilicate glass properties

PyrogelIXT: insulation material used in storage tanks to minimize thermal losses.

Property	Value (T expressed in °C)
Density [kg/m^3]	100
Thermal conductivity [W/(m · K)]	$2.7778 \cdot 10^{-10} \cdot T^3 - 3.2143 \cdot 10^{-8}$ $\cdot T^2 + 3.4484 \cdot 10^{-5} \cdot T + 0.019905$
Specific heat capacity [J/(kg · K)]	1046

Table B.5: PyrogelIXT properties

Concrete: material constituting the storage basement.

Property	Value
Density [kg/m^3]	1860
Thermal conductivity [W/(m · K)]	0.72
Specific heat capacity [J/(kg · K)]	780

Table B.6: Concrete properties

Air: constitutes the gas layer trapped inside the two storage tanks between the molten salts' free surface and the top of the tank.

Property	Value (T expressed in K)
Density [kg/m^3]	$3.492 \cdot 10^{-2}/T$
Dynamic viscosity [Pa · s]	$3.177 \cdot 10^{-8} \cdot T + 1.052 \cdot 10^{-5}$
Thermal conductivity [W/(m · K)]	$5.512 \cdot 10^{-5} \cdot T + 1.202 \cdot 10^{-2}$
Specific heat capacity [J/(kg · K)]	$1.947 \cdot 10^{-1} \cdot T + 9.411 \cdot 10^{2}$

Table B.7: Linearized ideal-gas air properties

Appendix C

Partanna solar field optical characterization

This appendix summarizes the optical data (IAM and reference efficiency) for the Partanna CSP plant.

Reference efficiency: it characterizes the solar field when the Sun is at the zenith, and its value is 0.704;

Incident Angle Modifier (IAM): it depends on both transversal and incident angles, and is provided in the table below:

Transversal/Incidence angle [°]	Transversal IAM	Longitudinal IAM
0	1.00	1.00
10	0.98	0.98
20	0.96	0.92
30	0.95	0.83
40	0.91	0.69
50	0.86	0.52
60	0.70	0.31
70	0.48	0.11
80	0.23	0.00
90	0.00	0.00

Table C.1: Transversal and longitudinal IAM for the Partanna CSP plant

Appendix D

09-06-2015 input trends

This appendix graphically represents the trends of the inputs used in the daily simulation of Section 3.4.1.

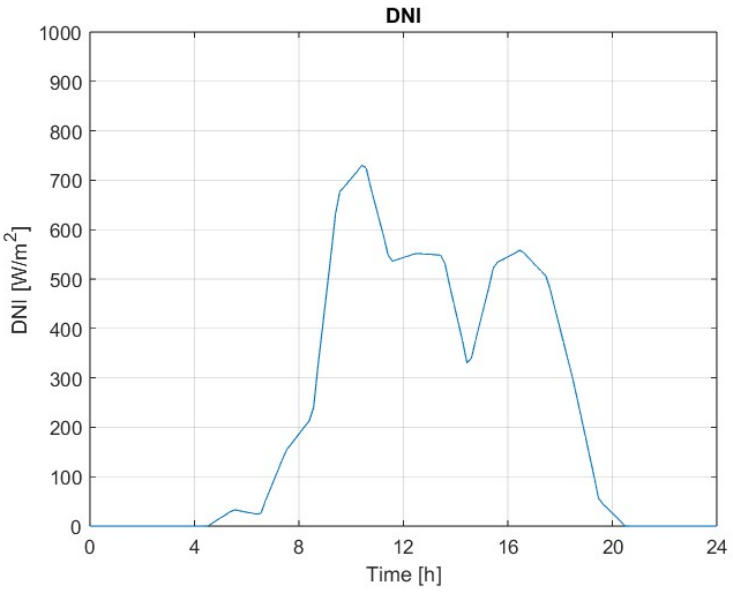

Figure D.1: Daily DNI

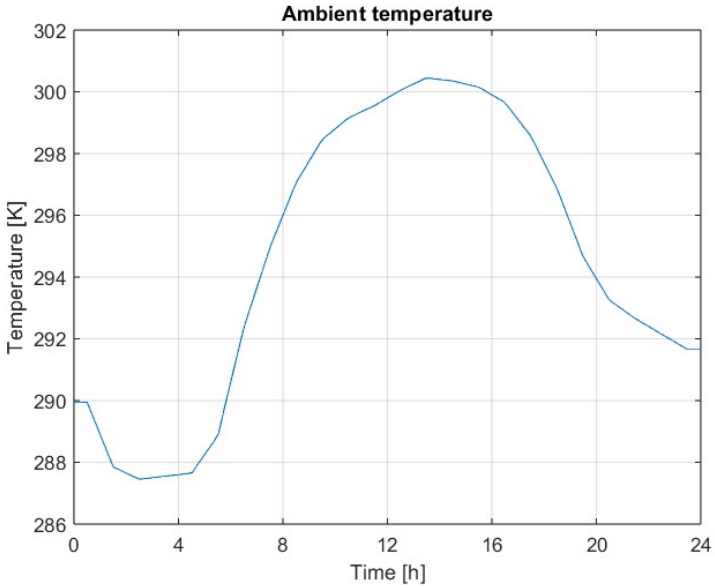

Figure D.2: Daily ambient temperature

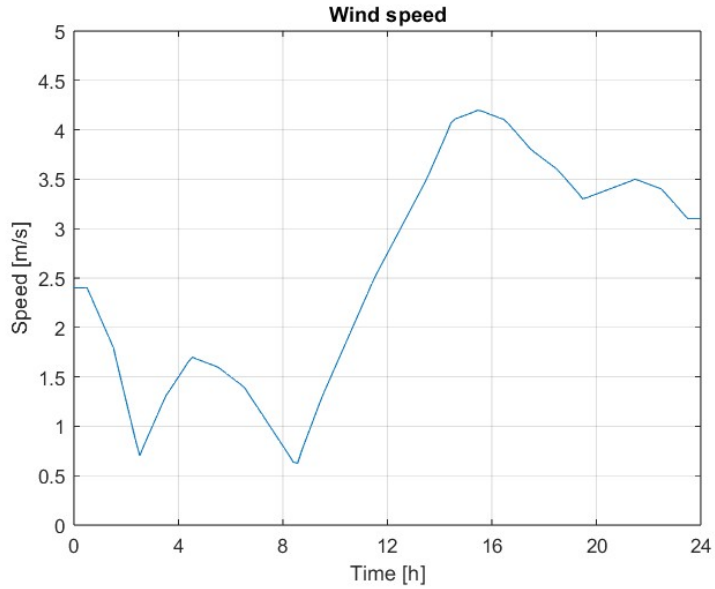

Figure D.3: Daily wind speed

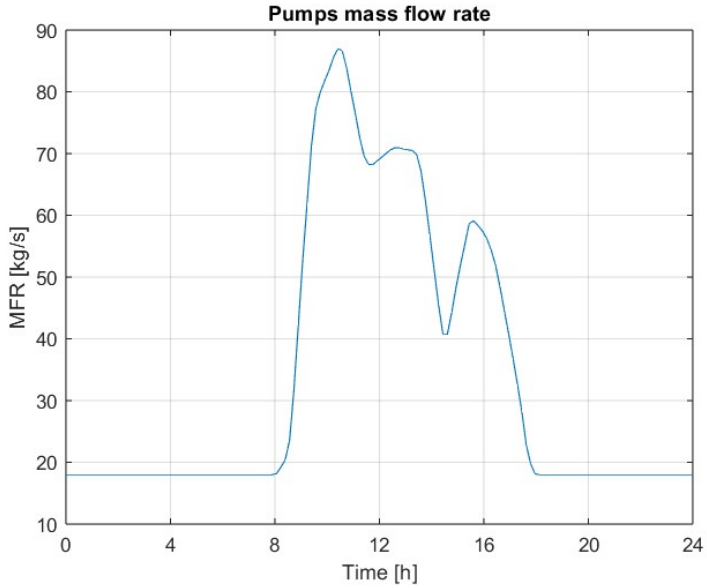

Figure D.4: Daily SB pump mass flow rate

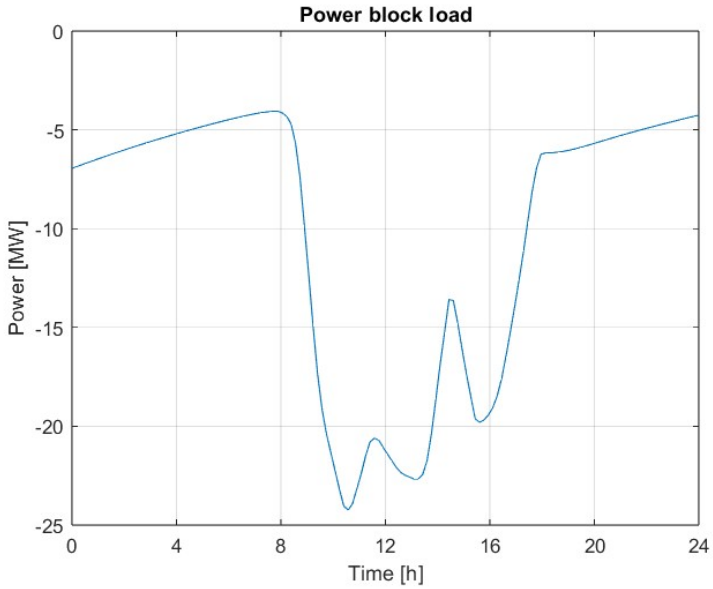

Figure D.5: Daily power load

Appendix E

Typical year input trends

This appendix graphically represents the trends of the inputs used in the daily simulation of Section 3.4.2.

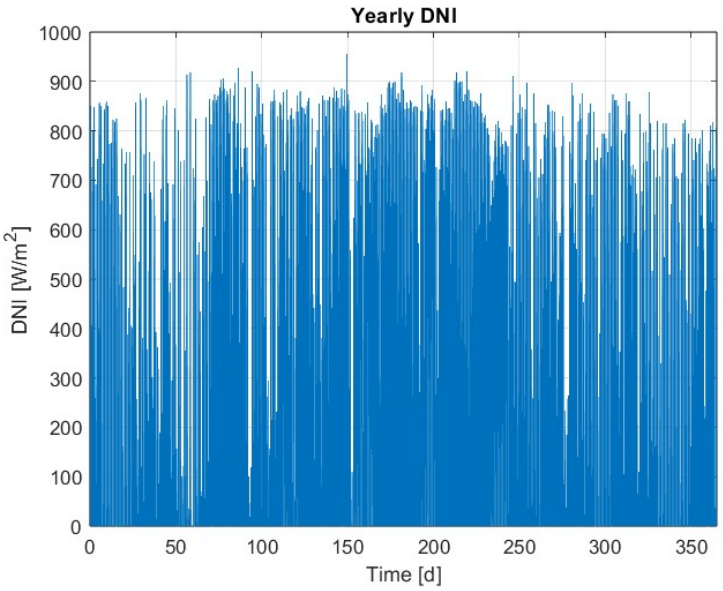

Figure E.1: Yearly DNI

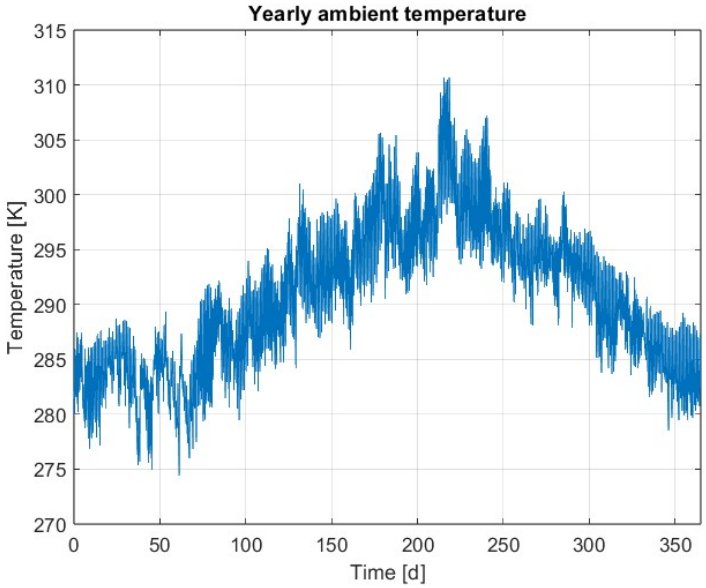

Figure E.2: Yearly ambient temperature

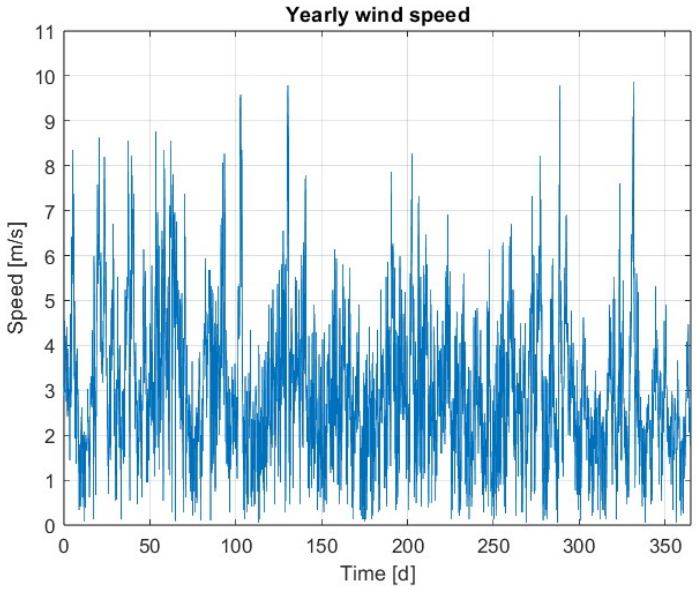

Figure E.3: Yearly wind speed

Appendix F

Linear CSP plants economic data

This appendix provides the economic data used in the Partanna CSP plant techno-economic evaluation.

Parameter	Value
LFC solar field (EUR/m^2)	138
Evacuation of the tube (EUR/m)	32
Site improvement (EUR/m^2)	18
HTF system (EUR/m^2)	43
Power block (EUR/kWe)	1010
TES system (EUR/kWht)	29
PV solar field (EUR/kW$_p$)	3000
Contingency (% of direct cost)	7
EPC and owner cost (% of direct cost)	10
Discount rate	0.1
Useful life of the plant (years)	30
Annual cost of operation and maintenance (% of CAPEX)	2

Table F.1: Linear CSP plants economic data for LCOE analysis [1] [17]

[1] Currency exchange rate (20 August 2023): EUR 1.00 = USD 1.09

Bibliography

[1] International Energy Agency. "Technology Roadmap - Concentrating Solar Power". In: *IEA Publications* (2010).

[2] Modelica Association. *Modelica*. URL: `https://modelica.org/` (visited on 02/10/2025).

[3] Modelica Association. *Open Modelica*. URL: `https://openmodelica.org/` (visited on 02/10/2025).

[4] Theodore L. Bergman et al. *Fundamentals of Heat and Mass Transfer*. John Wiley & Sons, 2011.

[5] Mattia Cagnoli. *Optical and Thermal-Fluid-Dynamic Modelling of the Solar Loop of CSP Systems Based on the PT or the LFR Technology*. Tech. rep. Politecnico di Torino, 2019.

[6] Mattia Cagnoli and Roberto Zanino. "An Introduction to Concentrated Solar Power (CSP) Technology". Solar Thermal Technologies PoliTo course lecture notes.

[7] Gianni Comini and Giovanni Cortella. *Fondamenti di Trasmissione del Calore*. Servizi Grafici Editioriali, 2017.

[8] Gianni Comini and Stefano Savino. *Fondamenti Termodinamici dell' Energetica*. Servizi Grafici Editioriali, 2020.

[9] European Commission. *PVGIS*. URL: `https://re.jrc.ec.europa.eu/pvg_tools/en/` (visited on 02/24/2025).

[10] World Bank Group. *Global Solar Atlas*. URL: `https://globalsolaratlas.info/map` (visited on 03/04/2025).

[11] Matthias Günther. "Advanced CSP Teaching Materials - Linear Fresnel Technology". German Aerospace Center material on enerMENA project.

[12] Matthias Günther. "Advanced CSP Teaching Materials - Solar Radiation". German Aerospace Center material on enerMENA project.

[13] Matthias Günther, Michael Joemann, and Simon Csambor. "Advanced CSP Teaching Materials - Parabolic Trough Technology". German Aerospace Center material on enerMENA project.

[14] Corporate Finance Institute. *Levelized Cost of Energy (LCOE)*. URL: https://corporatefinanceinstitute.com/resources/valuation/levelized-cost-of-energy-lcoe/ (visited on 02/27/2025).

[15] L. Pilotti et al. "Simultaneous design and operational optimization of hybrid CSP-PV plants". In: *Applied Energy* (2022).

[16] Johannes Sattler, Bryan O'Connell, and Daniel Norton. "Advanced CSP Teaching Materials - Solar Tower Technology". German Aerospace Center material on enerMENA project.

[17] Mehdi Shokrnia et al. "Comparative Techno-Economic Analysis of Parabolic Trough and Linear Fresnel Collectors with Evacuated and Non-Evacuated Receiver Tubes in Different Geographical Regions". In: *Processes* (2024).

[18] Filippo Spertino. "The Current-Voltage (I-U) Characteristic Curve: Effect of Irradiance and Temperature". Solar Photovoltaic Systems PoliTo course lecture notes.

[19] Statista. *Total primary energy supply worldwide in 2022 with a forecast for 2030 to 2050 in a 1.5°C scenario, by source*. URL: https://www.statista.com/statistics/801881/global-total-energy-supply-by-source/ (visited on 03/03/2025).

[20] David Watts et al. "Potential residential PV development in Chile: The effect of Net Metering and Net Billing schemes for grid-connected PV systems". In: *Renewable and Sustainable Energy Reviews* (2014).

[21] Mohamed E. Zayed et al. "A comprehensive review on Dish/Stirling concentrated solar power systems: Design, optical and geometrical analyses, thermal performance assessment, and applications". In: *Journal of Cleaner Production* (2020).